NARPEX project

Final Report

Silke Groß[1], Florian Ewald[1]

[1] Deutsches Zentrum für Luft- und Raumfahrt, Institut für Physik der Atmosphäre, Münchner Str. 20, 82234 Oberpfaffenhofen, Germany

ESA Contract No. 4000117782/16/NL/FF/mg
Earthcare Pre-Launch Campaigns Activity:
NARVAL Processing Experiment (NARPEX)

FINAL

Content

ACRONYMS & ABBREVIATIONS

CALIOP	Cloud-Aerosol Lidar with Orthogonal Polarization
CALIPSO	Cloud-Aerosol Lidar and Infrared Pathfinder Satellite Observations
D_{eq}	Equivalent melted diameter
DLR	Deutsches Zentrum für Luft- und Raumfahrt
EarthCARE	Earth Cloud Aerosol Radiation Explorer
ECMWF	European Center for Medium-range Weather Forecast
HALO	High Altitude and Long-range research aircraft
HAMP	HALO Microwave Package
HSRL	High Spectral Resolution Lidar
IWC	Ice Water Content
IWP	Ice Water Path
LUT	Look up table
NARPEX	NARVAL Processing Experiment
NARVAL	Next-generation aircraft remote sensing for validation studies
NWP	Numerical weather prediction
OD	Optical Depth / Optical Thickness
PIP	Process Implementation Plan
PSD	Particle size distribution
RASTA	Radar system airborne
REFF	Effective radius
SEVIRI	Spinning enhanced visible and infrared imager
WALES	Water Vapor Lidar Experiment in Space

1. INTRODUCTION / OVERVIEW

This document describes the work performed in the frame of the NARVAL Processing Experiment (NARPEX) in preparation of the EarthCARE mission. It covers the tasks in response to the Statement of Work (SoW) from ESA (EOP-SM/2925/DS-ds of 18 April 2016) with substitutions of Task 4 as proposed and agreed on in September 2017.

The overall objectives of the NARVAL Preprocessing Experiment (NARPEX) project are derived from the scientific goals, objectives and needs in the framework of the Earth Explorer mission EarthCARE. The aim of NARPEX is to enable the generation of products supporting future campaign activities and to develop first ideas for scientific calibration/validation of the EarthCARE mission. The NARVAL Processing experiment will support the consolidation of Lidar/Radar instrumentation operations together with enhanced data processing capabilities and quality control procedures to support the demonstration of validation capabilities for EarthCARE in:

1. Development and tests of methods and strategies for validation studies based on coordinated HALO and A-Train Radar and Lidar measurements
2. Sensitivity of airborne and spaceborne Radar and Lidar measurements considering different wavelengths for both kinds of measurements.
3. Development and test of methods for future synergetic Radar and Lidar EarthCAREdata inversion.

NARPEX builds on previous work deploying the DLR differential absorption and high spectral resolution lidar WALES and the Cloud Radar MIRA36 on the HALO research aircraft during the NARVAL mission in 2013 and 2014. The NARVAL payload combines, amongst others, an airborne lidar and an airborne radar system onboard the HALO aircraft. With this instrumentation NARVAL measurements provide similar data as will be derived from future EarthCARE measurements. To achieve these above mentioned objectives the following work has been performed:

- Analysis of performed A-Train underpasses and comparison of satellite and airborne measurements, e.g. to investigate the potential of satellite measurements to be used to study small scale cloud structures, to evaluate differences of satellite and airborne radar and lidar measurements.
- Test and application of synergistic analysis retrieval; we applied the variational optimal estimation retrieval VarCloud.
- Specify differences in different radar-lidar retrieval algorithm versions and investigate the resulting differences in the derived microphysical products, i.e. differences in the operational retrieval on A-Train and the research retrieval VarCloud.
- Investigating differences in radar and lidar data based on the use of different wavelengths.

2. NARVAL PROJECT AND DATA

2.1 NARVAL

The general objective of NARVAL (Next-generation Aircraft Remote Sensing for Validation Studies) was to demonstrate the performance of the NARVAL remote sensing payload (see Section 2.3) onboard the German High Altitude and Long-range (HALO) aircraft for different tasks of research and in different regions. Therefore, two measurements campaigns (NARVAL South / NARVAL North) were conducted in the subtropical/tropical and in the extratropical Northern Atlantic region in December 2013 and January 2014, respectively.

NARVAL South:

NARVAL South took place between 10 and 20 December 2013 with its main focus

- to obtain cloud statistics for trade wind clouds, e.g. to study the transition between non-precipitating and precipitating shallow convection
- to study the temporal evolution of an air mass and its clouds
- to compare HALO observations with collocated A-train satellite data

Overall eight research flights (Figure 1) were performed during NARVAL South. Half of the research flights were performed as transfer flights between Oberpfaffenhofen and Barbados to characterize the transfer from mid-latitudes to the tropics; the other half was performed as local flights out of Barbados to characterize the variability within the trade wind region in the vicinity of the Caribbean.

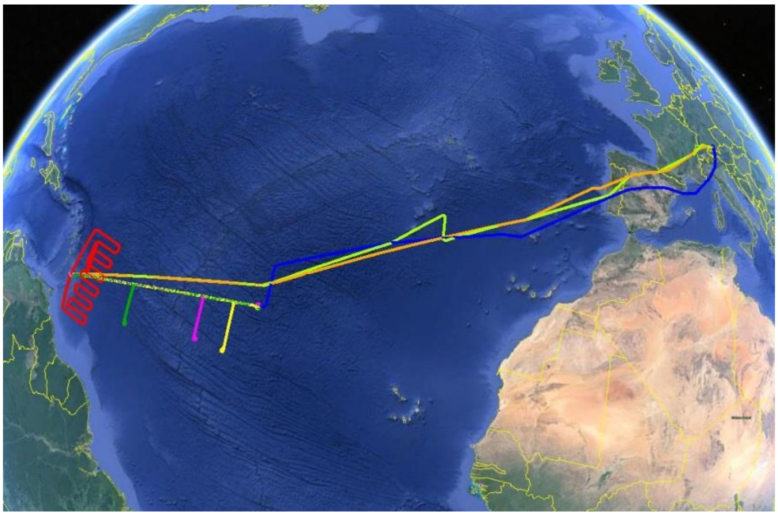

Figure 1: Flight tracks for NARVAL South flights.

During the NARVAL South flights seven Cloudsat/CALIPSO underflights were conducted. An overview of the performed NARVAL South research flights including times of take-off, landing and CALIPSO underflights is given in Table 7.

Table 1: Conducted research flights during NARVAL South. OBF stands for the airport in Oberpfaffenhofen; BGI stands for the airport on Barbados. All times are given in UTC.

Flight No.	Date	Type	Take-off	Landing	Underflight
RF01	10/12/13	Transfer	10:14 (OBF)	20:41 (BGI)	15:08
RF02	11/12/13	Local	14:29 (BGI)	21:58 (BGI)	17:26
RF03	12/12/13	Local	13:50 (BGI)	20:20 (BGI)	16:30
RF04	14/12/13	Local	13:35 (BGI)	20:21 (BGI)	16:18
RF05	15/12/13	Local	15:15 (BGI)	21:45 (BGI)	17:01
RF06	16/12/13	Transfer	13:10 (BGI)	22:59 (BGI)	16:07
RF07	19/12/13	Transfer	10:05 (OBF)	19:57 (BGI)	
RF08	20/12/13	Transfer	16:20 (BGI)	02:35 (OBF)	17:19

Another highlight during the NARVAL South flights was a coordinated flight with the French Falcon F20 which was equipped with a cloud radar at 95 GHz to compare the effects of different wavelengths for cloud studies and retrievals.

NARVAL North:

NARVAL North was conducted between 7 and 22 January 2014 out of Iceland. Five local Figure 2) and two transfer flights were performed with the main objectives:

- to characterize convective mesoscale postfrontal precipitation in the greater outflow region of the Labrador Sea
- to identify deficits of existing satellite and NWP data to detect such systems that can lead to unpredicted high impact weather over Europe
- to compare HALO observations with collocated A-train satellite data

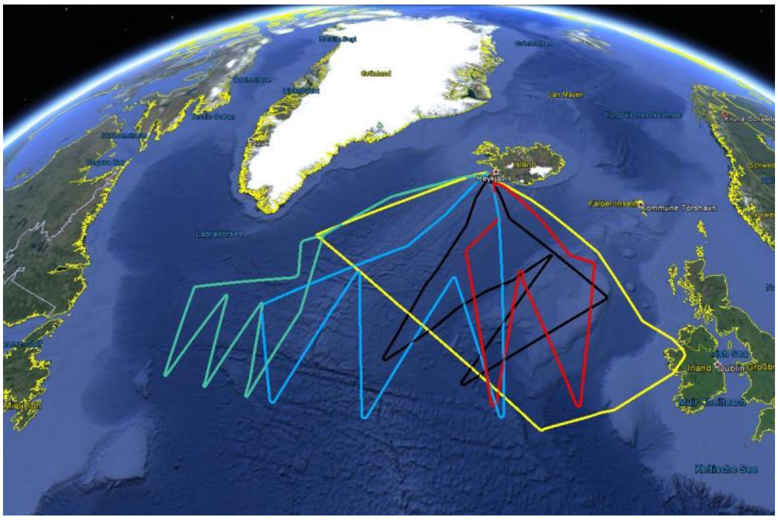

Figure 2: Flight tracks of NARVAL North research flights.

During NARVAL North three Cloudsat/CALIPSO underflights were conducted. An overview of the performed NARVAL North research flights including times of take-off, landing and CALIPSO underflights is given in Table 2.

Table 2: Conducted research flights during NARVAL North. OBF stands for the airport in Oberpfaffenhofen; KEF stands for the airport Keflavik on Iceland. All times are given in UTC.

Flight No.	Date	Type	Take-off	Landing	Underflight
TF01	07/01/14	Transfer	12:08 (OBF)	17:50 (KEF)	
RF01	09/01/14	Local	08:14 (KEF)	17:20 (KEF)	15:28
RF02	12/01/14	Local	08:32 (KEF)	15:10 (KEF)	
RF03	18/01/14	Local	08:55 (KEF)	14:49 (KEF)	13:44
RF04	20/01/14	Local	10:15 (KEF)	18:45 (KEF)	
RF05	21/01/14	Local	10:52 (KEF)	17:00 (KEF)	14:19
TF02	22/01/14	Transfer	10:02 (KEF)	14:25 (KEF)	

Additional measurements are available from three test flights over Germany in June and July 2013, including one coordinated measurement flight with CALIPSO/Cloudsat.

2.2 HALO aircraft

During NARVAL the German high altitude and long-range research aircraft HALO (Figure 3) was be employed. HALO is a modified Gulfstream G550 business jet with an endurance of more than 10 flight hours, a maximum range of about 8000 km, and a maximum cruising altitude of more than 15 km.

Figure 3: HALO (High Altitude and LOng range) aircraft. Photo adopted from http://www.halo.dlr.de/.

2.3 NARVAL payload

During NARVAL HALO was equipped with an extensive set of active and passive remote sensing instruments combining radar and lidar measurements together on one aircraft (Figure 4) and thus provide EarthCARE like measurements that can be used for preparation studies with respect to the EarthCARE mission. Dropsondes completed the measurement setup.

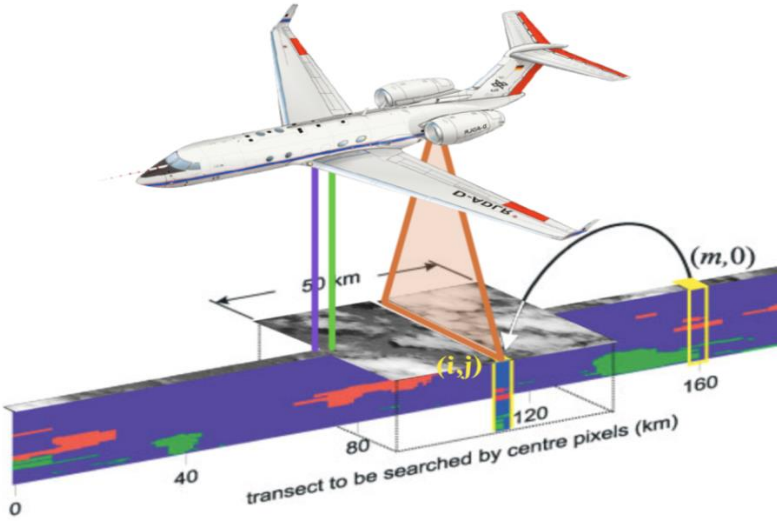

Figure 4: Sketch of HALO measurements with NARVAL instrumentation (imaging measurements available since 2016). Figure adopted from Barker et al.., 2011.

Information of responsibility and data products of the different instruments / instrument packages are listed in Table 3. Data from the grey shaded instrumentation in Table 3 will partly be used for the NARPEX project and is explained in more detail in the following.

Table 3: Instrumentation employed during the NARVAL campaign, responsibility and data product. Grey shaded instrumentation will partly be used for the proposed study, and is partly explained in more detail in the following.

Instrument	Responsibility	Data product
HAMP	MPI-M, UniHH, Uni Köln in cooperation with DLR-PA	Liquid water path, temperature + humidity profiles, cloud snow + rain water path, profiles of radar reflectivity, depol. Ratio + vertical velocity
WALES	DLR-PA	Profiles of water vapour, backscatter coefficient at 532 nm and 1064 nm, color ratio of backscatter (532 nm / 1064 nm), particle linear depolarization ratio at 532 nm and 1064 nm, particle extinction coefficient at 532 nm, real time quicklooks
HALO-SR	Uni Leipzig	Irradiance, radiance, actinic flux densities
miniDOAS	Uni Heidelberg	H2O, CO2, CH4, NO2, HONO, BROx, ClOx, IOx, HCHO, SO2, O3
Dropsondes	DLR-PA, in cooperation with MPI-M, UniHH	Profiles of relative humidity, temperature and horizontal wind velocity

2.4 WALES

The lidar system WALES (Figure 5) is a combined differential absorption and high spectral resolution lidar (HSRL) system developed and built at the Deutsches Zentrum für Luft- und Raumfahrt (Wirth et al., 2009; Esselborn et al., 2008).

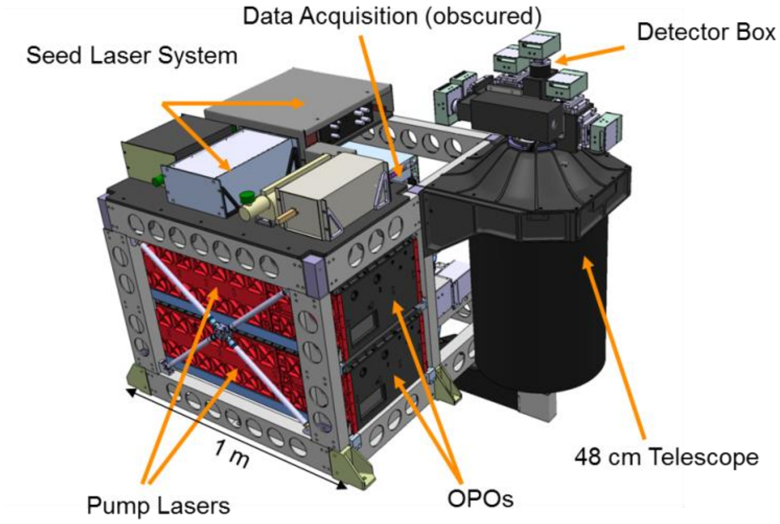

Figure 5: Sketch of the WALES lidar system

The WALES lidar system consists of two transmitters, both based on an injection-seeded optical parametric oscillator (OPO) pumped by the second harmonic of a Q-switched, diode pumped Nd:YAG laser. WALES is capable to nearly simultaneously emit four wavelengths, three online and one offline, in the water vapour absorption band between 935 and 936 nm. The three online wavelengths achieve the necessary sensitivity needed for measurements over the whole range of tropospheric water vapour concentration. A complete water vapour profile of the troposphere is composed by using the information of the partly overlapping line contributions. The single pulse energy at 935 nm is 35 mJ with a repetition rate of 200 Hz (or 50 Hz for each quadruple). The vertical resolution of the raw data is 15 m. In addition to the 935 nm channel, the receiver is equipped with polarization-sensitive aerosol channels at 532 and 1064 nm, the first one with High Spectral Resolution capabilities using an iodine filter in the detection path (Esselborn et al., 2008). Typical transmitted pulse energies are 60 mJ at 532 nm and 120 mJ at 1064 nm. This allows for collocated measurements of humidity and optical depth, as well as studies of clouds and aerosol optical properties.

2.5 MIRA36

MIRA36 is a commercial standard METEK Ka-band (36 GHz) cloud radar with polarization and Doppler capability to determine vertical velocity in clouds and precipitation. Together with microwave radiometers in the K-, V-, W-, F-, and G-band the MIRA36 is part of the HALO microwave package (HAMP) (Mech et al., 2014). Technical details are summarized in Table 4.

Table 4: System parameters of the MIRA36 cloud radar

Frequency	35.5 GHz
Peak Power	35 kW
Diameter of Antenna	1.1 m
Antenna Beam Width	0.5 deg.
Sensitivity at 5 km	-44.5 dBZ

2.6 Auxiliary data

To derive backscatter coefficient and backscatter ratio from the WALES lidar measurements auxiliary information on temperature and pressure are mandatory. For the data processing of WALES model analysis data from ECMWF is used. This data is interpolated in space and time to match the WALES measurements.

2.7 NARPEX data

Based on the high spectral resolution lidar (HSRL) measurements on HALO and co-located A-Train satellite data the following data products shall be retrieved:

- Attenuated lidar backscatter signals
- Profiles of Radar reflectivity (Z)

Furthermore the coordinated flight with the French Falcon F20 will be evaluated.

3. DATA PROCESSING AND STRUCTURE

3.1 Basic of WALES Data Processing

As the light pulse emitted from a lidar propagates through the atmosphere its intensity is reduced by scattering and absorption by the molecular constituents of the air and by aerosol and cloud particles. Part of the light is also scattered in a backward direction and propagates back to the lidar system, again undergoing the same extinction process. In this way the signal of a lidar depends on the local ability of the atmosphere to scatter light and on the integral light extinction along the complete light path between the system and the probed volume. This can be seen in a more formal way from the so called lidar equation, which gives the power P received from an atmospheric volume at distance r:

$$\mathrm{P(r)} = \left(\frac{\mathrm{E_0 c}}{2} \cdot \frac{\mathrm{A}}{\mathrm{r^2}}\right) \cdot \left(\beta_\mathrm{m}(\mathrm{r}) \cdot \mathrm{T_a^2(r)} + \beta_\mathrm{p}(\mathrm{r}) \cdot \mathrm{T_a^2(r)}\right)$$

Here the first term in brackets contains system-specific parameters: the laser pulse energy E_0 and the area of the receiving telescope A (c is the speed of light). The atmospheric parameters are described by the backscatter coefficients for light scattering from air molecules β_m and particles β_p as well as the total atmospheric transmission T_a from the system to the probed volume. For a monochromatic light source and in the absence of multiple scattering T_a can be written in the form (Beer´s law):

$$\mathrm{T_a\,(r)} = \exp\left(\int_0^{\mathrm{r}} \left(\alpha_\mathrm{m}(\mathrm{r'}) + \alpha_\mathrm{p}(\mathrm{r'})\right) \cdot \mathrm{dr'}\right)$$

where $\alpha_m(r)$ and $\alpha_p(r)$ are the molecular or particle extinction coefficients.

The molecular coefficients β_m and α_m are proportional to the air density and can be calculated from the molecular scattering cross-sections obtained from laboratory measurements and the pressure and temperature profile from numerical weather prediction (NWP) models or independent collocated measurements, e.g., from radiosondes.

In sharp contrast to the molecular case, the coefficients describing light scattering by particles β_p and α_p are extremely sensitive to the size, shape and refractive index of the particles. Especially there is no simple general relation between the two parameters, as for molecular (Rayleigh) scattering. The HSRL method uses the fact that air molecules have a much lower mass and therefore a much higher thermal velocity than aerosol or cloud particles. This high random velocity leads to a significant spectral broadening of the laser light scattered by the molecules due to the Doppler Effect. If plotted against the wavelength shift, the spectrum of the light scattered back to the lidar receiver looks like the dashed curve shown in Figure 6. It consists of a broad, nearly Gaussian-shaped part coming from scattering by molecules and a narrow central peak from particle scattering.

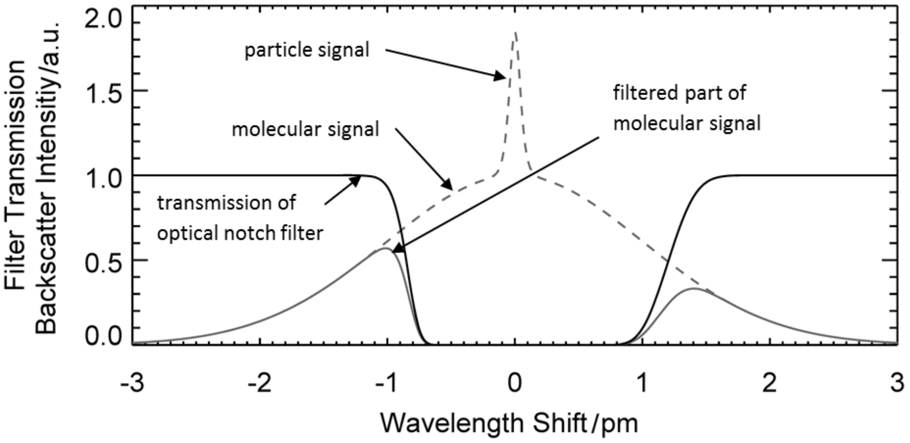

Figure 6: Spectral signatures of the light backscattered from the atmosphere. Figure adapted from Groß et al., 2012.

Using HSRL the received atmospheric backscatter is split into two channels. The narrow bandwidth optical filter in the molecular channel suppresses the aerosol backscatter, whereas the combined channel detects the intensity of both aerosol and molecular backscatter. Therefore the emitted laser frequency must be tuned to match the filter absorption line. The iodine absorption filter eliminates the aerosol backscatter and transmits the wings of the Doppler broadened molecular backscatter spectrum. To determine the amount of molecular backscatter absorbed by the iodine filter, the HSRL system needs to be calibrated. This is done by measuring the filter transmission spectrum and calculating the atmospheric temperature and pressure-dependent filter transmission with an appropriate molecular backscatter model. For measuring the iodine filter transmission spectrum, a highly attenuated reflection of the pulsed green laser emission is directed through the receiver assembly and the laser frequency is scanned. The filter transmission is determined by the product of the iodine filter transmission and the calculated molecular backscatter spectrum.

The lidar equation for the filtered signal is then reduced to the first term:

$$P_{HSRL}(r) = C \cdot \left(\frac{E_0 c}{2} \cdot \frac{A}{r^2}\right) \cdot \beta_m(r) \cdot T_a^2(r)$$

where the calibration constant C accounts for the fact that also part of the molecular scattered light is rejected by the notch filter. The big advantage of this reduced equation is that from the particle scattering parameters it only contains α_p (wrapped into T_a). Since all other parameters are known or can be calculated with good accuracy, the atmospheric transmission between the lidar and an arbitrary point along the laser beam can be directly measured. From this data product it is straightforward to calculate α_p by simple numerical differentiation with a relative systematic error of typically less than 5%. Since we not only want to measure the extinction coefficient α_p but also the backscatter coefficient β_p the signal in a HSRL receiver is split into two parts, one for the total signal and one with the optical notch filter. As the transmission from the HSRL channel is known, the lidar equation can be solved for β_p.

Uncertainties

Systematic errors in the measurement of the backscatter coefficient arise from uncertainties of the measured quantities and the calculated quantities are mainly due to normalization, where the magnitude of background aerosol at a reference height within the free troposphere has to be estimated. The assumption of the background backscatter coefficient is based on the analysis of in situ measured aerosol size distributions. Further uncertainties are induced by laser frequency fluctuations and variations in the atmospheric temperature.

3.2 Basic of MIRA Data Processing

The processing of cloud radar I-Q-signals to calibrated radar reflectivity includes the following steps:

Calculation of FFT power spectra in each range gate

Received pulses are sampled with the range sampling period of 15 m, 30 m, or 60 m depending on the transmitted pulse length – 100 ns, 200 ns, or 400 ns, respectively. Samples of the received pulses from a given range gate produce a complex signal, sampled with the pulse repetition frequency of 5 kHz. By the complex notation, the signal can be written as:

$$y(kT) = I(kT) + iQ(kT), \quad k = 0, 1, \ldots, N_{FFT} - 1.$$

$y(kT)$ is called “I-Q-signal”, and T is the pulse repetition period. $N_{FFT} = 256$ is the length of the Fast Fourier Transform (FFT). Subsequently, the power spectrum $p(N_{FFT})$ from $y(kT)$ is calculated.

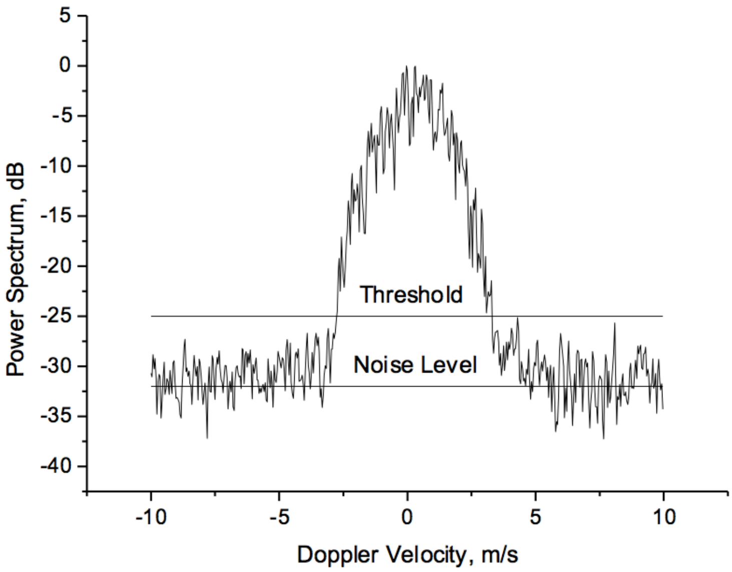

Figure 7: Power spectrum of the Doppler velocity.

Non-coherent averaging of FFT power spectra

Before peak identification and moment estimation are performed, $K_{sum} = 20$ power spectra are averaged non-coherently to improve the signal-to-noise ratio.

Estimation of signal moments

The Doppler velocity v and signal power PR can be estimated from the power spectrum of the scattered signal.

The threshold value S_{TH} used to separate the signal S_n and the noise parts of the spectrum is calculated from the noise power P_N (with Q=7). While the mean Doppler velocity v results from the 1st moment of S_n the signal power P_R is the 0st moment of S_n:

$$S_{TH} = < N_n > + Q \cdot \sigma_{SUM}(N_n) = \frac{P_N}{N_{FFT}}\left(1 + \frac{Q}{\sqrt{K_{SUM}}}\right).$$

$$S_n = \begin{cases} S[k] - S_{NL}, & S_n \geq S_{TH}, \\ 0, & S_n < S_{TH}. \end{cases}$$

$$v = -\frac{\lambda}{2}\frac{1}{P_0}\sum_{n=0}^{N_{FFT}-1} f_n S_n, \qquad P_R = \sum_{n=0}^{N_{FFT}-1} S_n.$$

Calculation of calibrated radar reflectivity

After that, the SNR is calculated by dividing P_R by the receiver noise level:

$$SNR = 10\log\left(\frac{P_R}{P_{RecNoise}}\right)$$

Here, the noise power P_{RecNoise} is obtained from the noise gate. The equivalent radar reflectivity factor Z_e is then calculated from the estimated *SNR* values using the radar equation for meteorological radars:

$$Z_e = C_0 \left(\frac{H}{H_0} \right)^2 \frac{F}{F_0} \frac{\tau_0 P_{TAV0}}{\tau \, P_{TAV}} SNR$$

For convenience, following reference values were used here (H_0 = 5 km, P_{TAV0} = 30 W, F_0 = 5 kHz, and t_0 = 200 ns). Using the radar parameters listed in the following table, the specific radar constant C_0 is -26.1 dB:

$$C_0 = \frac{1024 \ln 2 \lambda^2 K_B T_0}{\pi^3 c |K_w|^2} 10^{18} \frac{L F_N}{G_0^2 \theta_0^2} \frac{F_0 H_0^2}{P_{TAV0} \tau_0}$$

Radiometric calibration of the MIRA cloud radar

In order to provide scientifically sound interpretations of cloud radar measurements, a well-calibrated instrument with known sensitivity is indispensable. Many space- or ground-borne techniques to retrieve cloud microphysics using millimeter-wave radar measurements require a calibration uncertainty of around 1dB or better. (Protat et. al (2009))

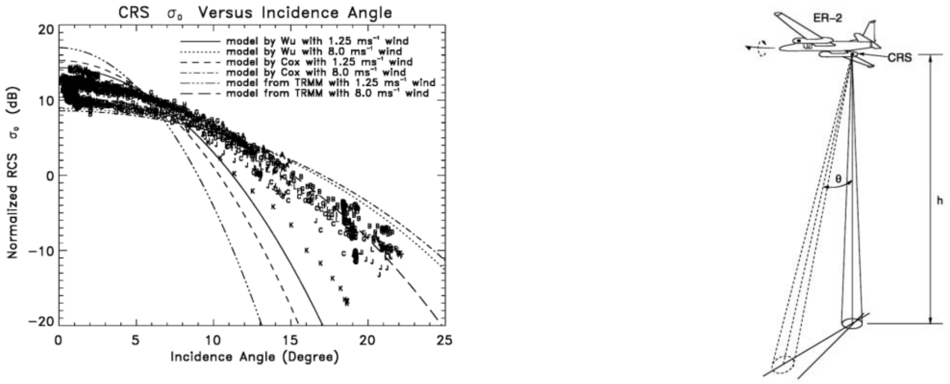

Figure 8 (left) Normalized Radar Cross Sections measured by Li et al. (2005) as a function of beam incidence angle with modelled NRCS for various surface wind speeds. (right) Measurement principle for the plot on the left, where the aircrafts executes alternating roll maneuvers to sample the NRCS for different beam incident angles.

Li et al. (2005) demonstrated the radiometric absolute calibration of an airborne cloud radar by using the ocean surface backscatter. Figure 8 illustrates the calibration principle where measured Normalized Radar Cross Sections (NRCS) for different beam incident angles are compared to modeled NRCS. During the follow-up campaign NARVAL2 in 2016, alternating roll maneuvers were executed to apply the same technique to the cloud radar MIRA. Additionally, the radar receiver has been recalibrated by DLR in the lab. Here, a systematic bias of -8 dB has been found for the manufacturer calibration. It is likely, that this bias is also present in identical ground-based cloud radars from this manufacturer. With the new calibration (green in Figure 9, left), the NRCS now fit much better to the values predicted by the model (dashed line). Moreover, NCRS now agree also well to measured NCRS by the Global Precipitation

Measurement satellite (blue triangles). Furthermore, this calibration bias turned out to be the largest error in a Radar/Lidar retrieval of ice cloud microphysics.

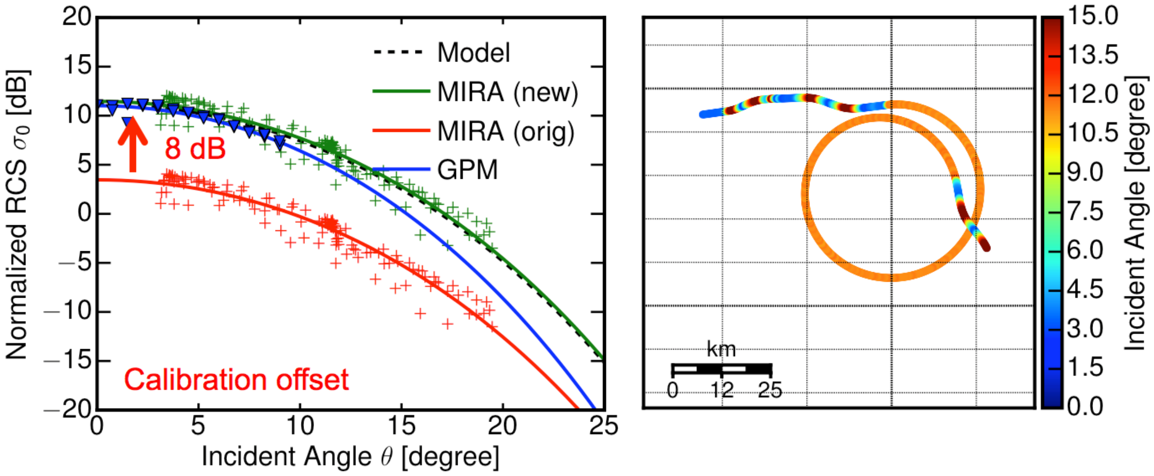

Figure 9 (left) Measured Normalized Radar Cross Sections returned by the sea surface. The red crosses correspond to the manufacturer calibration, the green crosses to the new calibration and the blue triangles represent measurements from the GPM satellite. (right) Radar calibration flight pattern with alternating roll maneuvers and a 10 degree bank circle.

3.3 File Description for MIRA36

```
typedef netCDF //netCDF data format
YYYYMMDD_hhmm.mmclx {
dimensions:
      time  = UNLIMITED ; // (25078 currently)
      range = 487 ;
variables:
[…]
      float SNRg(time, range) ;
            SNRg:long_name = "Reflectivity SNRg" ;
            SNRg:units = " " ;
            SNRg:yrange = -22.90047f, 70.f ;
            SNRg:db = 1s ;
      float VELg(time, range) ;
            VELg:long_name = "Doppler Velocity VELg" ;
            VELg:units = "m/s" ;
            VELg:yrange = -12.66761f, 12.66761f ;
            VELg:db = 0s ;
      float RMSg(time, range) ;
            RMSg:long_name = "Peak Width RMSg" ;
            RMSg:units = "m/s" ;
            RMSg:yrange = 0.f, 3.f ;
            RMSg:db = 0s ;
      float LDRg(time, range) ;
            LDRg:long_name = "Linear De-Polarization Ratio LDRg" ;
            LDRg:units = " " ;
            LDRg:yrange = -35.f, 5.f ;
            LDRg:db = 1s ;
      float SNRcx(time, range) ;
            SNRcx:long_name = "Reflectivity SNR Cx-Channel" ;
            SNRcx:units = " " ;
            SNRcx:yrange = -35.f, 70.f ;
            SNRcx:db = 1s ;
      float Ze(time, range) ;
            Ze:long_name = "Equivalent Radar Reflectivity Factor Ze of
            Hydrometeors" ;
            Ze:units = "Z" ;
            Ze:yrange = -60.f, 30.f ;
            Ze:db = 1s ;
      float Zg(time, range) ;
            Zg:long_name = "Equivalent Radar Reflectivity Factor Ze of all
            Targets" ;
            Zg:units = "Z" ;
            Zg:yrange = -60.f, 30.f ;
            Zg:db = 1s ;
      float RadarConst(time) ;
            RadarConst:long_name = "Radar Constant related to 5 km Height, and
            200 ns pulses. Z = SNR * RadarConst * (range/5 km)^2 * SNRCorFaCo. It
            changes slightly in time due to the measured transmit power" ;
            RadarConst:units = "Z" ;
            RadarConst:yrange = -35.f, -20.f ;
            RadarConst:db = 1s ;
```

3.4 File Description for WALES

```
typedef netCDF //netCDF data format
YYYYMMDDhhmmss_ADLR_WVDIAL_BACKSC_D_V1.0.nc {
dimensions:
      time  = UNLIMITED ; // (18240 currently)
      range = 859 ;
variables:
      double time(time) ;
            time:long_name ="seconds since 1970-01-01 00:00:00 00:00 UTC";
            time:units = "seconds since 1970-01-01 00:00:00 00:00 UTC" ;
      double time_resolution(time) ;
            time_resolution:long_name = "time resolutions" ;
            time_resolution:units = "s" ;
      float height_above_sea_level(time) ;
            height_above_sea_level:long_name = "height_above_sea_level" ;
            height_above_sea_level:units = "m" ;
            height_above_sea_level:missing_value = -9.e+33f ;
            height_above_sea_level:_FillValue = -9.e+33f ;
      float latitude(time) ;
            latitude:long_name = "latitude" ;
            latitude:units = "degree_north" ;
            latitude:standard_name = "latitude" ;
      float longitude(time) ;
            longitude:long_name = "longitude" ;
            longitude:units = "degree_east" ;
            longitude:standard_name = "longitude" ;
      float range(range) ;
            range:long_name = "range" ;
            range:units = "m" ;
            range:standard_name = "range" ;
      float range_resolution(time, range) ;
            range_resolution:long_name = "range_resolution" ;
            range_resolution:units = "m" ;
            range_resolution:standard_name = "vertical_resolution" ;
      float emission_wavelength;
            emission_wavelength:long_name = "emission_wavelength" ;
            emission_wavelength:units = "nanometer" ;
            emission_wavelength:standard_name = "emission_wavelength" ;
      float instrument_elevation_angle(time) ;
            instrument_elevation_angle:long_name = "elevation" ;
            instrument_elevation_angle:units = "degree" ;
            instrument_elevation_angle:description = "elevation angle from
            -90 to +90 degrees" ;
            instrument_elevation_angle:missing_value = -9.e+33f ;
            instrument_elevation_angle:_FillValue = -9.e+33f ;
      float backscatter_due_to_aerosol(time, range) ;
            backscatter_due_to_aerosol:long_name = "backscatter
            coefficient at 532 nm" ;
            backscatter_due_to_aerosol:units = "m-1 sr-1" ;
            backscatter_due_to_aerosol:missing_value = -9.e+33f ;
            backscatter_due_to_aerosol:_FillValue = -9.e+33f ;
```

4. SYNERGISTIC RADAR AND LIDAR ANALYSIS

4.1 Synergistic radar-lidar retrieval

The combination of radar and lidar measurements on one platform provides two advantages (Figure 10):

1) As a consequence of the different wavelengths used for the radar and lidar measurements they are sensitive to different particle sizes and thus complement one another. Lidar measurements are sensitive to small particle sizes and are thus an optimal tool for the characterization of aerosols and thin ice clouds. In contrast the radar is sensitive to larger particles and thus able to characterize clouds and precipitation.
2) By synergistically use of the radar and lidar measurements they provide information on cloud mask and microphysical cloud properties, e.g. the ice water content, the effective radius and the number concentration.

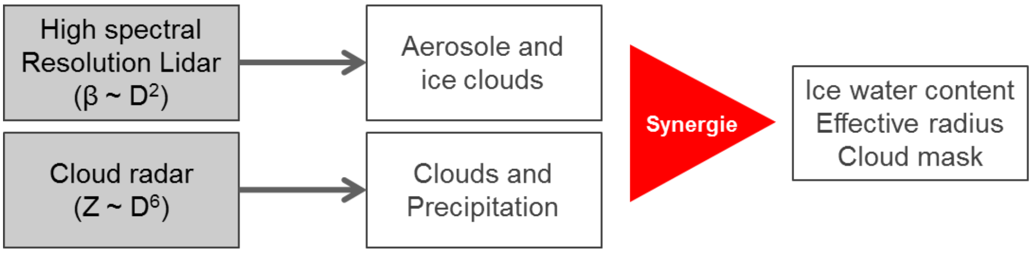

Figure 10: Theoretical scheme of the benefit of combined radar and lidar measurements.

The retrieval approach to synergistically combine radar and lidar measurements that is used in this study is based on a variational optimal estimation algorithm (Delanoë and Hogan, 2008). The unique characteristic of this approach is the rigorous application of an online forward model to simulate the multiple-scattering lidar signal together with the Jacobians to estimate a microphysical profile fitting radar and lidar.

Figure 11(a) shows the basic schematic of the variational optical estimation algorithm. Based on the meteorological condition (e.g. Temperature) a priori profiles of the extinction coefficient α, the extinction-to-backscatter ratio S, and the ice particle number concentration N are determined. These state profiles are used to forward model the instrument signals (i.e. attenuated backscatter coefficient β_π and radar reflectivity Z_e) in first guess. The forward-modeled radar and lidar profiles are than compared to the measured radar and lidar profiles. In iterative steps the state profiles are changed to better fit to the measurements until the forward-modeled instrument signals have converged with the measured attenuated backscatter coefficient and radar reflectivity (Figure 11(b) and (c)). The cloud microphysical properties (e.g. ice water content and cloud effective radius) are than derived from the actual state profile.

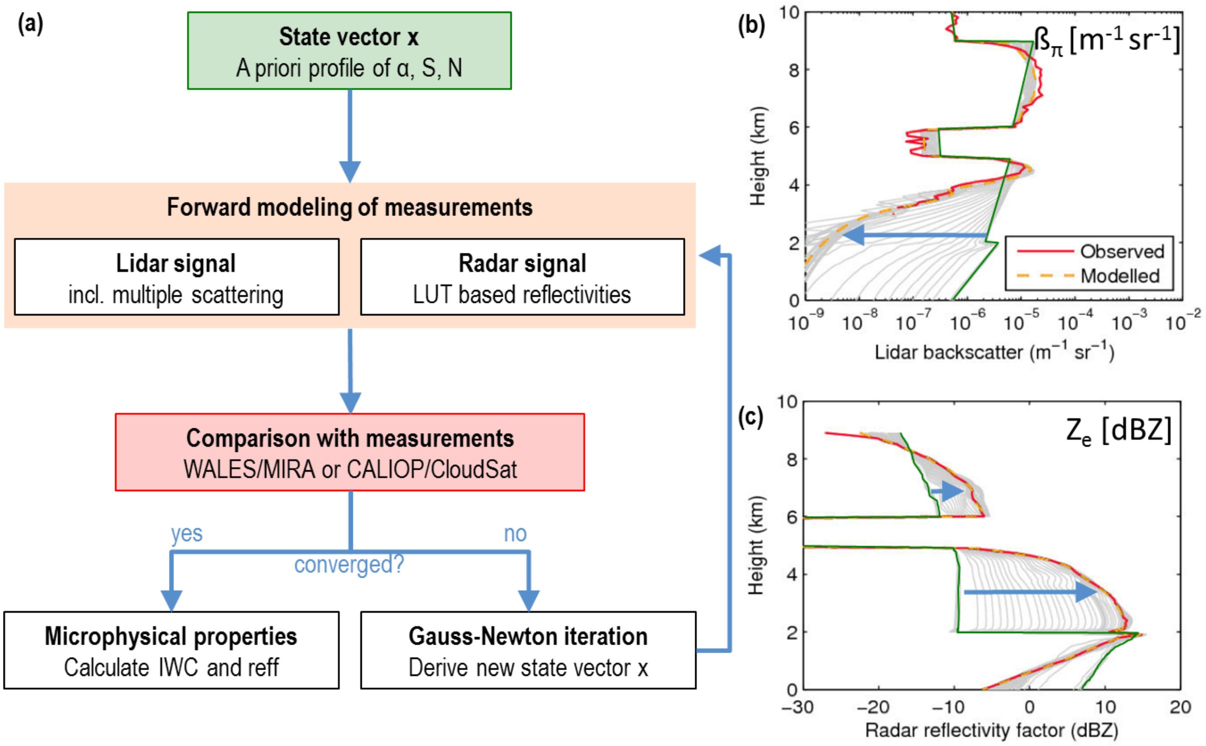

Figure 11: Scheme of variational optimal estimation algorithm (a), and example on synthetic backscatter coefficient (b) and radar reflectivity profiles (c).

Microphysical Assumptions

While active backscatter retrieval techniques surpass the information content of most passive, vertically integrated retrieval techniques, their accuracy is limited by essential assumptions about the ice crystal shape. To simplify the diversity of ice crystals, most radar-lidar retrieval algorithms rely on a mass- size relationship to parameterize the prevalent ice particle shape.

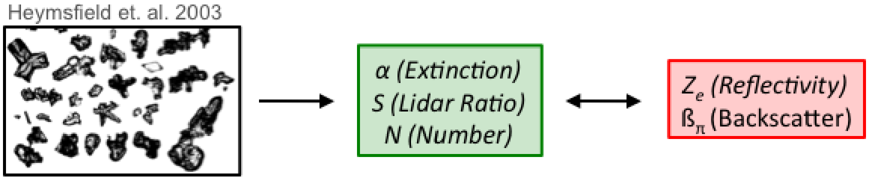

Figure 12: Generalization of in-situ measured ice particle shapes using extinction, lidar ratio and concentration number density. This parameterization reduces the complexity of ice particle shapes, which is essential to relate the microphysics of ice clouds with measured radar reflectivity Ze and lidar backscatter βπ.

Further essential prerequisites are assumptions about the ice particle size distribution and a-priori profiles of extinction α, lidar ratio S and ice concentration number N. In combination with the assumed mass-size relationship, these assumptions serve as input to forward models of radar and lidar signals:

- *Mass-Size Relationship M(D)*
- *Particle Size Distribution N(D)*
- *A-priori profiles N(T), S(T)*

Delanoë et al. (2005) developed the microphysical assumptions for the *VarCloud* algorithm. The core idea is a normalized particle size distribution, which is fitted to a large microphysical in situ database. In combination with the well-proven mass-size relationship of Brown and Francis (1995), this approach reduces the degrees of freedom from the infinite number of possible ice crystal shapes to the basic quantities of mean-volume diameter D_m and intercept parameter N_0^* (a normalized ice crystal number concentration). Delanoë et al. (2008) used this approach to implement the radar-lidar retrieval VarCloud, which operational version on the A-Train constellation is called DARDAR (VarCloud v2.1.1) and described by Delanoë et al. (2010).

As an improvement (VarCloud v3) of their approach, Delanoë et al. (2014) updated their microphysical assumptions using a very large in situ dataset including bulk measurements of IWC and direct measurements of the projected areas of the ice particles, a good proxy of visible extinction (Heymsfield et al., 2010). This section will briefly summarize the differences between the microphysical assumptions between DARDAR (VarCloud v2.1.1) and VarCloud v3.

In situ Dataset

The DARDAR algorithm relies on in-situ measurements of the ice particle size distribution N(D) from 2D-C (25 and 800 µm) and 2D-P (200 and 6400 µm) probes during several measurement campaigns (CLARE98, CARL99, ARM, EUREX, FASTEX). Delanoë et al. (2014) updated this dataset by the dataset described by Heymsfield et al. (2010) with in situ measurements covering a large variety of ice clouds from different geographical locations and campaigns (TC4, NAMMA, CF, ARM, MPACE, AIRS, C3VP, Subvisible). Here, the bulk measurement of IWC and the direct measurement of the projected ice particle area are key advantages to test the consistency of the fitted microphysical models.

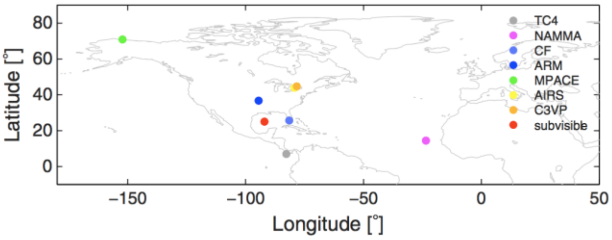

Figure 13: Global location of each field campaign (TC4, NAMMA, CRYSTAL-FACE, ARM, C3VP, AIRS, and Subvisible) for the in situ ensemble used within VarCloud.

Mass-Size Relationship M(D)

An important prerequisite of every ice cloud remote sensing retrieval is a microphysical ice crystal model. These models describe the relationship between particle size, particle mass and cross-sectional area using large in situ datasets. In VarCloud, the Mass-Size relationship of Brown and Francis (1995) and Mitchell et al. (1996) is used and formulated in terms of the mean particle dimension D. In all VarCloud versions (DARDAR and VarCloud v3), the ice particle mass and cross-sectional area for large ice crystals (D > 300 micron), is assumed to follow aggregates of unrimed radiating assemblages of plates, side planes, bullets and columns:

$$M(D) = 1.9241\, e^{-3}\, D^{1.9}$$

$$A(D) = 0.15189\, D^{1.64}$$

For smaller ice crystals (D < 300 micron), the relationship of *Mitchell et al. (1996)* for Hexagonal columns is used:

$$[100 < \mathrm{D} < 300 \text{ micron}]\ M(D) = 1.66\, e^{-3} D^{1.91}$$

$$[100 < \mathrm{D} < 300 \text{ micron}]\ A(D) = 0.0696\, D^{1.5}$$

$$[\mathrm{D} < 100 \text{ micron}]\ M(D) = 1.67\, e^{-1} D^{2.91}$$

$$[\mathrm{D} < 100 \text{ micron}]\ A(D) = 0.684 D^{2}$$

Note that D is in cm, A in cm^2 and M in g and that density and area are set to those for solid ice spheres when the implied density exceeds that for solid ice (0.92 g cm^{-3}). Following the simultaneous radar and in situ observations by Hogan et al. (2012), ice particles are treated as horizontally aligned oblate spheroids with an axial ratio of 0.6:

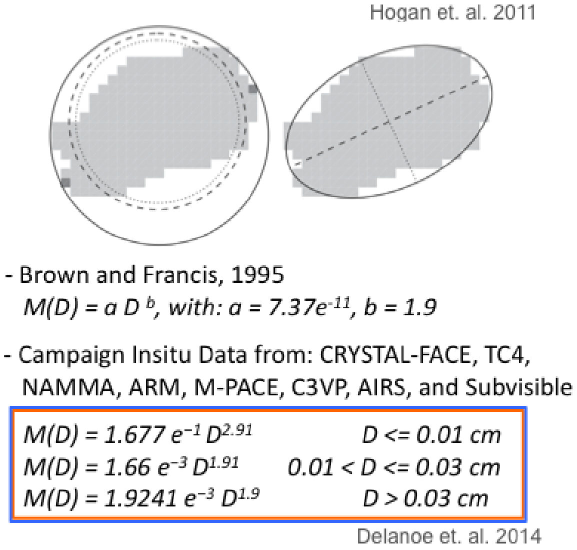

- Brown and Francis, 1995
  $M(D) = a\, D^{b}$, with: $a = 7.37e^{-11}$, $b = 1.9$
- Campaign Insitu Data from: CRYSTAL-FACE, TC4, NAMMA, ARM, M-PACE, C3VP, AIRS, and Subvisible

$M(D) = 1.677\, e^{-1} D^{2.91}$ $D <= 0.01$ cm
$M(D) = 1.66\, e^{-3} D^{1.91}$ $0.01 < D <= 0.03$ cm
$M(D) = 1.9241\, e^{-3} D^{1.9}$ $D > 0.03$ cm

Figure 14: Spheroid approximation of ice crystals using images from a 2D-C probe. Proposed by Hogan (2012), ice particles are assumed to be spheroids in VarCloud and DARDAR. On the left, the maximum dimension Dmax, the mean dimension Dmean, and the equivalent-area diameter Darea are shown for the fitted spheroid, while its major and minor axes are shown on the right.

Normalized particle size distribution (PSD) N(D)

In order to simplify the relationship between ice cloud microphysics and radar-lidar measurements, recent retrieval techniques (Delanoë et al., 2008; Szyrmer et al., 2012) use the normalized PSD approach. Testud et al. (2001) discovered that the very diverse PSDs in in situ measurements can be described by a modified gamma function when the diameter is normalized with the mean volume-weighted diameter D_m and the number concentration with the intercept parameter N_0^*. Delanoë et al. (2005) proposed the “unified” size distribution function *F:*

$$F(\alpha,\beta,X)=\beta\frac{\Gamma(4)}{4^4}\frac{\Gamma\left(\frac{\alpha+5}{\beta}\right)^{4+\alpha}}{\Gamma\left(\frac{\alpha+4}{\beta}\right)^{5+\alpha}}X^{\alpha}\exp\left[-\left(X\frac{\Gamma\left(\frac{\alpha+5}{\beta}\right)}{\Gamma\left(\frac{\alpha+4}{\beta}\right)}\right)^{\beta}\right],$$

The shape is defined as a function of the normalized size $X=D_{eq}/D_m$, which is defined as the quotient of melted-equivalent and mean volume-weighted diameter radius of the ice particle. The coefficients α and β allow fitting F to the shape of measured size distributions in the large in situ dataset. For DARDAR (v2.1.1), the dataset did not include direct IWC measurements, which made a closure study with the chosen M(D) impossible. Furthermore, this older dataset did not account for shattering of small particles. The updated VarCloud version (v3) is based on the extensive study by Delanoe et al. (2014), where the fitted coefficients α and β are checked to be consistent with simultaneous and direct measurements of IWC, visible extinction and radar reflectivity. In **Figure 15**, both PSD versions are compared to each other. While the DARDAR version (v2.1.1) still includes the very high number concentration of small particles caused by shattering, the new VarCloud version (v3) is corrected for this effect. The new coefficients α and β lead to a slightly broader size distribution, which now constrains the visible extinction of the analytical PSD to +-10% of the visible extinction of the actual measured PSD.

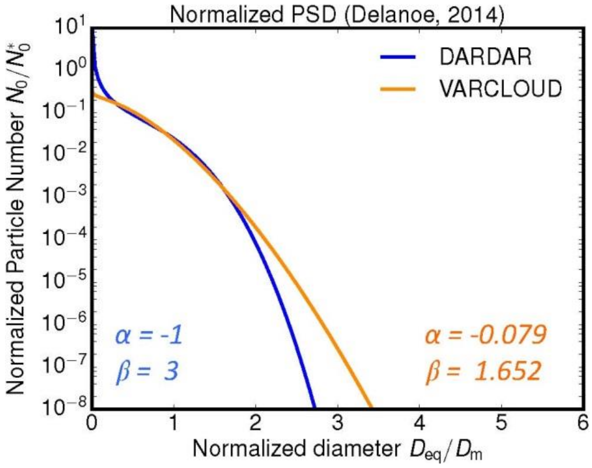

Figure 15: Idealized representation of the normalized PSD (modified gamma shape) used in DARDAR (blue) and VarCloud (orange). Delanoe (2014) obtained the coefficients α and β by using different in situ datasets, simultaneous measurements of visible extinction and radar reflectivity.

A-priori profiles for N(T) and S(T)

Further prerequisites of the iterative retrieval approach are good a-priori estimates of the state variables (normalized number concentration N', lidar ratio S and visible extinction α). This applies, in particular, in underdetermined regions where only radar or lidar is available. In these cases, the retrieval result is a combination of climatological information from the in situ data and one remote sensing instrument. In their normalized PSD paper, Delanoë et al. (2005) found a strong correlation with temperature T for the normalized number concentration parameter $N' = N_0^*/\alpha^{0.61}$. This additional normalization of the intercept parameter N_0^* with visible extinction α proved to be a vital step to exclude the influence of IWC on N_0^*. The analysis of the in situ dataset showed that *ln N'* increases linearly with temperature:

$$N' = N_0^* / \alpha^n$$

$$\ln N' = A_N + B_N T$$

While the lidar ratio S was assumed to be constant with height by Delanoë et al. (2008) and as a linear function of height in VarCloud version 1.2.1, Platt et al. (2002) already showed that *ln S* varies linearly with temperature. For this reason, the logarithm of the lidar ratio apriori in the current operational DARDAR (v2.1.1) and VarCloud (v3) version varies linearly with temperature T:

$$ln\ S = A_S - B_S T$$

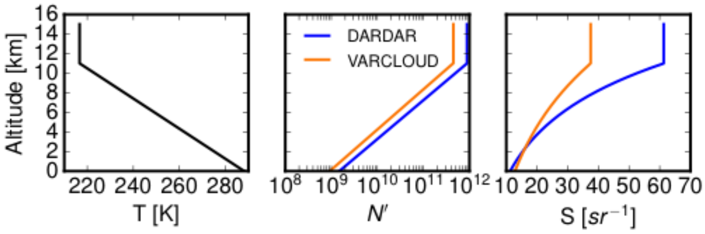

Figure 16: Temperature dependence of the apriori profiles of N' and S fitted to the in situ database of Delanoë et al. (2005) for DARDAR (blue) and Delanoë et al. (2014) for VarCloud (blue).

Due to the different extent of the in situ datasets, the fitted a-priori coefficients A_N, B_N, A_S and B_S differ between DARDAR (v2.1.1) and VarCloud (v3). Figure 16 compares the a-priori profile for N' and S for both versions in the case of a very simple temperature profile T. Here, the major difference can be found for the lidar ratio a-priori at low temperatures, where VarCloud (v3) assumes a much smaller, but more realistic lidar ratio.

A-priori	DARDAR (v2.1.1)	VarCloud (v3)
A_N	22.234435	21.94
B_N	-0.090736	-0.08647
A_S	2.7765	2.7765
B_S	0.0237	0.015
n	0.61	0.61

Table 5 Coefficients for the a-priori profiles for normalized number concentration N'(T) and lidar ratio S(T). The coefficients differ for DARDAR (v2.1.1) and VarCloud (v3) since they are based on a different in situ dataset.

4.2 Selected measurement case for synergistic analysis

To test the adapted synergistic radar-lidar retrieval on a real measurement case a flight leg during the NARVAL North measurements on 18 January 2014 is selected. The flight track is marked in Figure 17. The selected area (red line) is characterized by a high cirrus cloud layer located over Ireland. HALO headed in northward direction on its way back to Iceland.

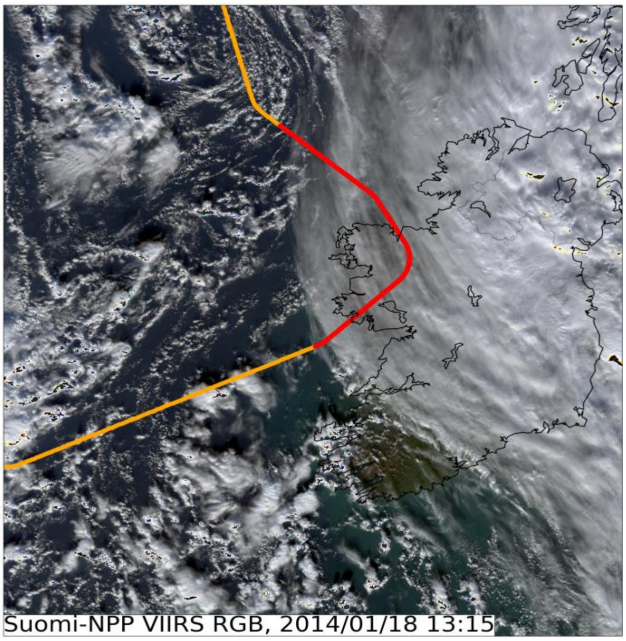

Figure 17: Suomi-NPP satellite image and HALO flight track for 18 January 2014. The red flight part marks the flight leg that was chosen for testing the synergistic radar-lidar retrieval.

A high pressure ridge moving in over the western North Atlantic narrowed the cold air trough that extended from Iceland over Ireland down to the Iberian Peninsula and into Northern Africa while a blocking situation continued over Europe. As a consequence the remains of a former low pressure system stayed in place mostly over Iceland and the British Islands as quasi stationary occlusion fronts that moved in several directions. On the western side of these low pressure systems the cold air flow started southward with a cloud-free area in the wake of the southern tip of Greenland. The convection started south of 60°N as shallow and stratiform cumulus first and rapidly developed into enhanced cumulus and Cumulonimbus offshore Ireland.

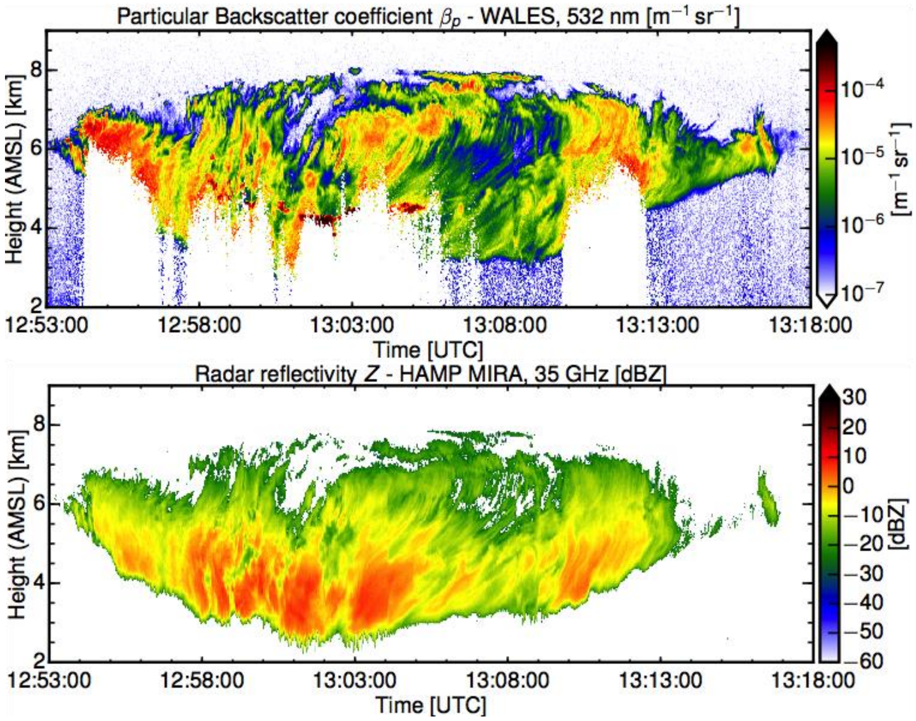

Figure 18: Lidar and radar measurements performed with WALES at 532 nm (upper panel) and with MIRA 36 at 36 GHz (lower panel) along the flight track on 18 January 2014 marked in red in Figure 17.

From the radar and lidar measurements (Figure 18) cloud structures from about 3 to 8 km height are obvious. Large values of the radar reflectivity are found in the lowermost part of the cloud between about 13:00 – 13:05 UTC in heights between about 3 and 5 km. The lidar signals get saturated in these regions of the cloud. Furthermore, one can see that parts of the cloud are missed by the radar observations. As both systems – the radar as well as the lidar – provide high quality measurements along this cirrus cloud influenced flight path, this measurement case is well suited to study the performance of synergistic radar-lidar retrievals.

4.3 Optimal measurement range for synergistic radar-lidar retrieval

The visualisation of the measurements in Figure 18 nicely shows the complementary measurement range of the two systems. While small scale structures on top of the cloud as well as cloud structures at the edge of the cirrus cloud are missed by the radar but seen by the lidar; the lidar gets saturated when the backscatter within the cirrus cloud becomes too strong so that the lowermost parts of the clouds are partly not covered by the lidar measurements while the radar is well suited to measure these parts of the cloud. The instrument mask shown in Figure 19 visualises which part of the cloud is detected by lidar only or radar only, and in which part of the cloud both systems provide good measurements. For the decision if the instrument detects the cloud we used a threshold of the backscatter ratio (i.e. ratio of the total backscatter coefficient to the molecular backscatter coefficient) of 1.25 for the lidar and of -60 dBZ for the radar.

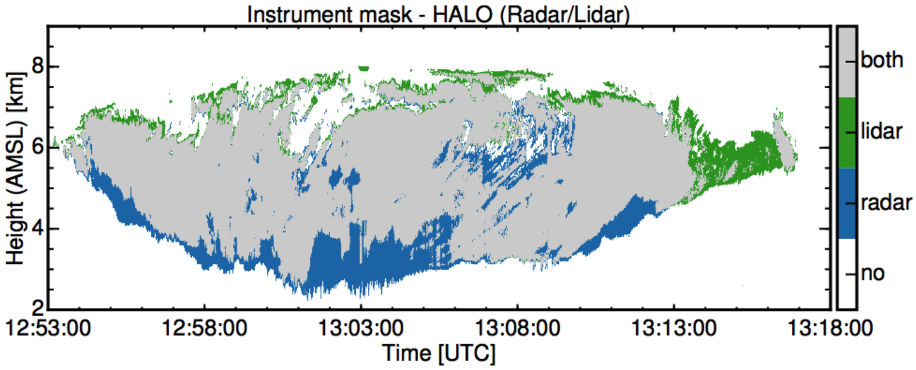

Figure 19: Instrument mask of radar and lidar measurements shown in Figure 18. Green colour indicates cloud regions with lidar observations only, blue colour indicates cloud regions with radar observations only, and grey colour indicates cloud regions with both – radar and lidar measurements.

To investigate the dependence of the saturation of the lidar measurements on the measured radar reflectivity we analyzed the frequency distribution (PDF) of the radar reflectivity inside the cloud (Figure 20). Looking of the overall PDF of the radar reflectivity we find a maximum and mean at about – 10 dBZ. Most of the observed dBZ values are found in a range between about -30 and about 5 dBZ. A small fraction of the observed dBZ values is found between about 5 – 10 dBZ. Looking at the parts of the cloud where we find good measurements of both instruments we see that the general shape of the distribution does not change significantly. However, no values > 10 dBZ are found. The maximum and the mean of the observed radar reflectivity in those parts of the cloud remain almost unchanged, compared to the PDF of the whole cloud, at a value of about -10 dBZ. Comparing now the PDF of the radar reflectivity of all parts of the cloud where we find radar only measurements we find a slightly larger distribution compared to the intersection of radar and lidar. Though the mean values remains almost constant we see a larger portion of observed radar reflectivity at the edges of the value range.

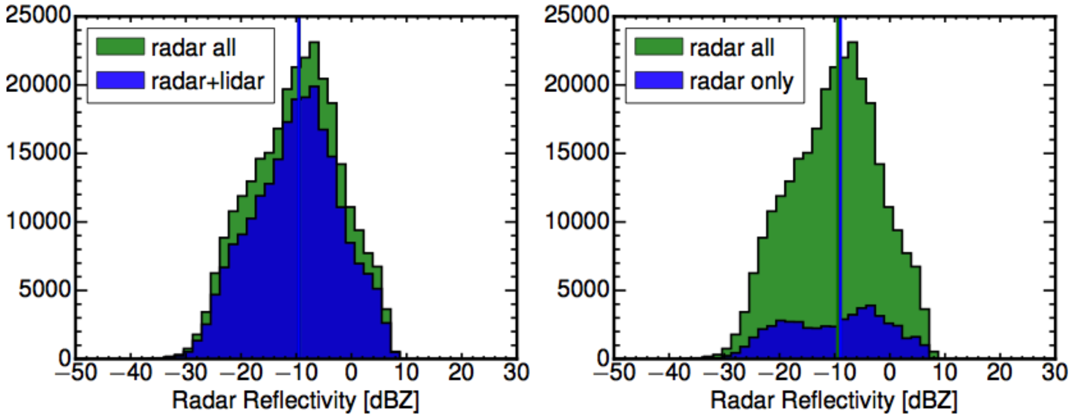

Figure 20: Absolute frequency distribution (PDF) of the radar reflectivity for the cloud scene shown in Figure 18. In the left plot the PDF of the radar reflectivity of all areas inside the cloud (green) and of the radar reflectivity of the parts of the cloud with simultaneous radar and lidar measurements (blue) are shown; in the right plot the PDF of all radar measurements inside the cloud (green) and the of radar only areas are shown.

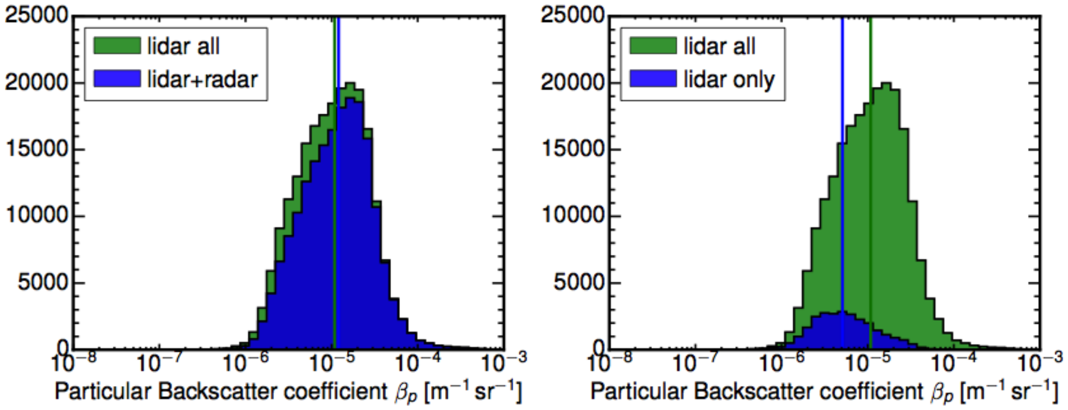

Figure 21: Same as Figure 20 but for the particular backscatter coefficient and 'lidar only' regions (left blue).

When we look now at the distribution of the backscatter coefficients measured by the lidar instrument we see a completely different behavior of cloud parts with intersection of lidar and radar and of parts with lidar only measurements (Figure 21). Taking all lidar measurements within the cloud into account we find an overall distribution of particulate backscatter coefficient (BSC) between about 2x10-6 and 1x10-3 m-1sr-1 although only a minor fraction of those measurements show values > 1x10-4 m-1sr-1. The maximum and mean of the PDF are at about 1x10-5 m-1sr-1. Taking now only the parts with intersection of lidar and radar we see that the overall maximum and mean of the PDF remains almost unchanged and that almost all BSC values larger than ~1x10-5 m-1sr-1 are measured in these parts of the cloud. While below this value both PDFs show the largest deviations. Especially the local maximum at about 2x10-6 m-1sr-1 is not visible in the intersections parts of radar and lidar. This local maximum almost completely arises from parts of the cloud where we find 'lidar only' measurements. Considering now only these parts of the cloud we again see that the range of BSC values is mainly limited to values small ~1x10-5 m-1sr-1. The maximum and the mean of this PDF are found at the local maximum of the overall PDF at about 2x10-6 m-1sr-1.

4.4 Influence of radar calibration and assumptions on retrieval results

Applying the synergistic analysis algorithm results in the retrieved ice water content (IWC) and effective radius (REFF) of the cloud scene presented in Figure 17 and Figure 18.

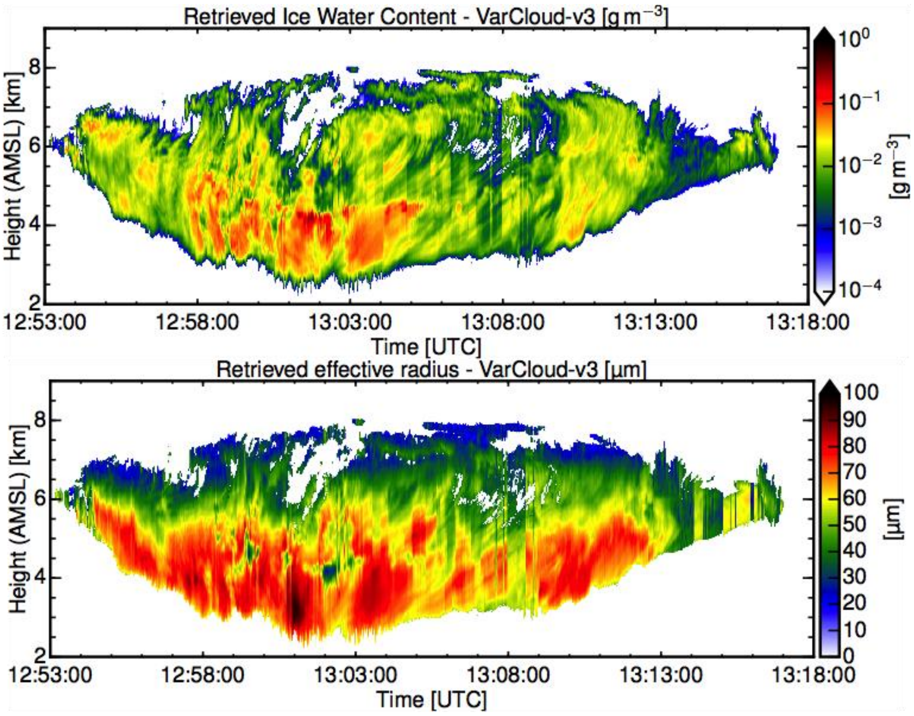

Figure 22 Retrieved ice water content and effective radius from the radar and lidar measurements shown in Figure 18 using VarCloud-v3

Most regions in the cloud show IWC values between ~1.5 µg/m^3 and ~25 µg/m^3. Very high IWC values are found in the lower part of the cloud where the lidar signal becomes saturated and radar measurements show the highest values of radar reflectivity of between -5 and 5 dBZ. REFF shows in general two regimes within the observed cloud. Small REFF are found in the upper part of the cloud with REFF between about 10 to 20 µm. These parts of the cloud are missed by radar observations while the lidar is well suitable to observe the parts of the cloud with small REFF. In the lower part of the cloud REFF is larger with values between about 50 to 70 µm. Very large values of up to ~75 µm are found in regions with a high radar reflectivity.

In a next study, the influence of the recalibrated radar data and the influence of different microphysical assumptions are compared between VarCloud-v3 and DARDAR-v2.1.1. To this end, the operational version of DARDAR (v2.1.1) (see page 20 for differences) is applied to the same scene. In addition, VarCloud-v3 is also run using radar data with the old, original calibration (with had an offset of -8.3 dB in Ze), which is called VarCloud-v3-8dB. By this way, the impact of different retrieval versions can be compared to the impact of a correct radar calibration. In Figure 23, relative frequency distributions of IWC (left) and REFF (right) are shown and compared between VarCloud-v3 (green) and DARDAR-v2.1.1 (blue).

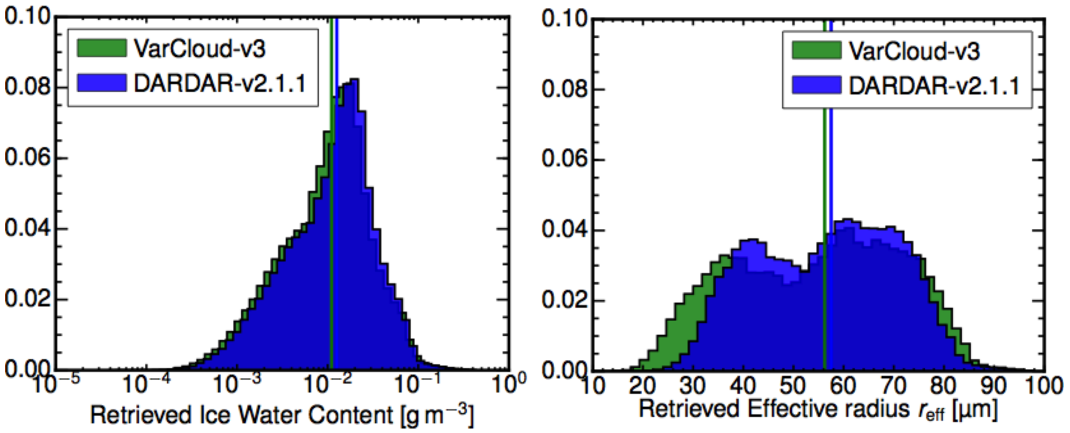

Figure 23: Relative frequency distributions of the retrieved ice water content and effective radius from radar and lidar measurements on HALO for the case in Figure 22 using the microphysical assumptions of VarCloud-v3 (green) and the assumptions of DARDAR-v2.1.1 (blue)

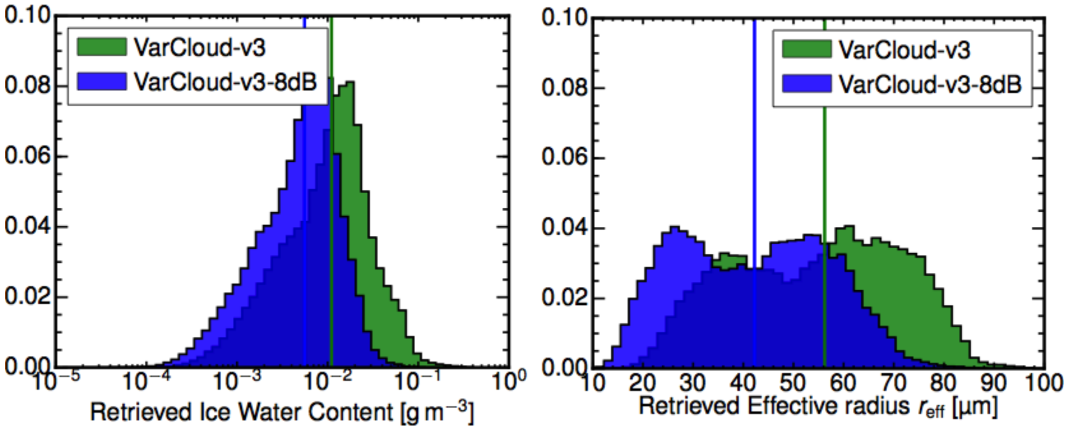

Figure 24: Relative frequency distributions of the retrieved ice water content and effective radius from radar and lidar measurements on HALO for the case in Figure 22 using the recalibrated MIRA data (green) and the original calibration (blue) using VarCloud-v3

We still see a good agreement in the retrieved properties applying different versions of the algorithm. VarCloud-v3 shows only a slightly broader value range for REFF than DARDAR-v2.1.1, but the overall REFF mean value for both algorithms agree well at around 55-60 µm. The REFF distributions for both versions show a two modal structure with a first maximum at about 40 µm and a second maximum at about 65 µm. For the IWC, almost no difference can be observed between both algorithm versions. This is in strong contrast, to the influence of the different radar calibrations. In Figure 24, relative frequency distributions of IWC (left) and REFF (right) are shown and compared between VarCloud-v3 using recalibrated radar data (green) and VarCloud-v3-8dB using the original radar calibration (blue). While the shape and width of the distributions of IWC and REFF remain almost identical, both are shifted towards smaller values. With the 8 dB lower radar reflectivity, the mean IWC shifts from $1x10^{-2}$ gm^{-3} to $5x10^{-3}$ gm^{-3} while the mean REFF decreases from 56 µm to 42 µm. Assuming Rayleigh scattering, this decrease corresponds to a decrease in radar reflectivity of $(56/42)^6 + 1/0,5$ = 7.6 dB which is in line with the actual 8.3 dB difference in radar reflectivity.

In a next step we compare the integrated properties (IWP and OD) along the flight track and look how the use of different versions of the algorithm and the recalibration of the cloud radar affects these properties. Figure 25 shows ice water path (upper plots) and optical thickness (lower plots) for the retrieval shown in Figure 22, comparing different retrieval versions (left plots) and different radar calibrations (right plots). Like in Figure 24, the different retrieval versions do not differ much. In contrast, the radar calibration offset of -8.3 dB causes a strong low bias in IWP and OD. For OD<1.0, the radar calibration offset causes an OD bias of up to -30%, while it is -50% or larger for OD>3. This increasing offset is caused by the missing lidar data at larger ODs, which helps to constrain the extinction at lower OD.

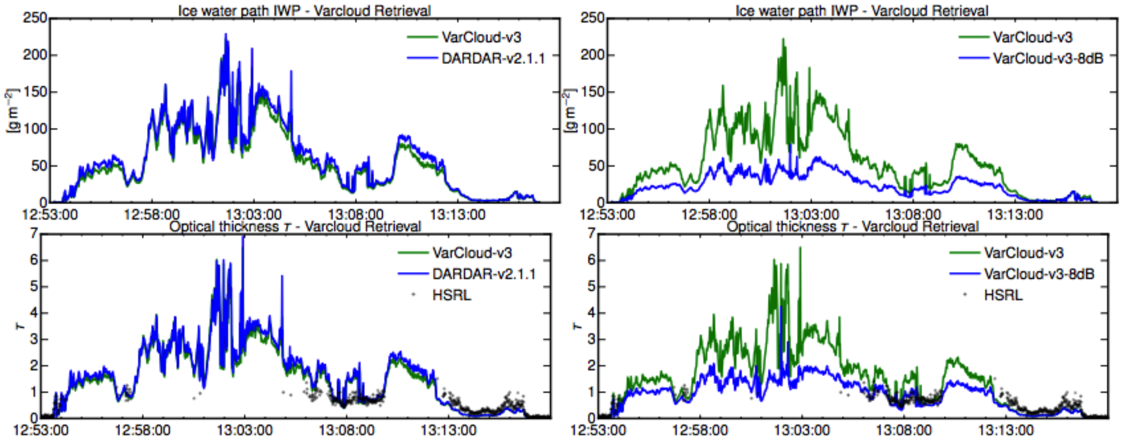

Figure 25 Retrieved ice water path (upper plot) and optical thickness (lower plot) derived from HALO and A-Train measurements as shown in Figure 22. The left plots compare the IWP and OD using the same version of the algorithm; for the right plots the operational DARDAR algorithm is used for CALIPSO and Cloudsat measurements.

5. SENSITIVITY STUDIES

Spaceborne measurements are usually performed with lower height and spatial resolution than airborne measurements. For example the Cloud-Aerosol Lidar with Orthogonal Polarization CALIOP on board CALIPSO (Winker et al., 2009) has an effective spatial resolution of about 330 m with an vertical resolution of 30 m. In contrast the WALES lidar system has a vertical resolution of 15 m and a temporal resolution of 0.1 s which corresponds to a horizontal resolution of about 22 m taking the usual aircraft speed of about 220 m/s into account. To determine the expected benefit and constraints of future EarthCARE measurements we use measurements of the current spaceborne lidar and radar systems on board CALIPSO and Cloudsat (Stephens et al., and compare them to the NARVAL lidar and radar measurements on board HALO. Therefore the following main topics are defined.

5.1 Applicability to study shallow marine convection

Shallow marine cumuli contribute about 60% to the net cloud radiative forcing and are one of the dominant contributors to global albedo (Hartmann et al., 1992). They cover about 12% of the sky over the Earth’s oceans (Warren et al., 1986), but are extremely variable in spatial extent with time. A large number of field experiments were conducted to better characterize shallow marine trade wind convection for numerical atmospheric models. Ground-based, shipborne or airborne measurements during field campaigns provide highly resolved observations of the macro- and microphysical cloud properties but are limited in space and time. Satellite measurements provide global coverage and long-term observations but the footprint of passive satellite observations mostly exceeds the small scale structure of trade wind convection. In contrast, spaceborne lidar measurements as they are performed on board CALIPSO or will be performed on board EarthCARE provide a much better spatial resolution. However, up to now no systematic evaluations of the applicability and constraints of spaceborne lidar measurements to study shallow marine convection have been done.

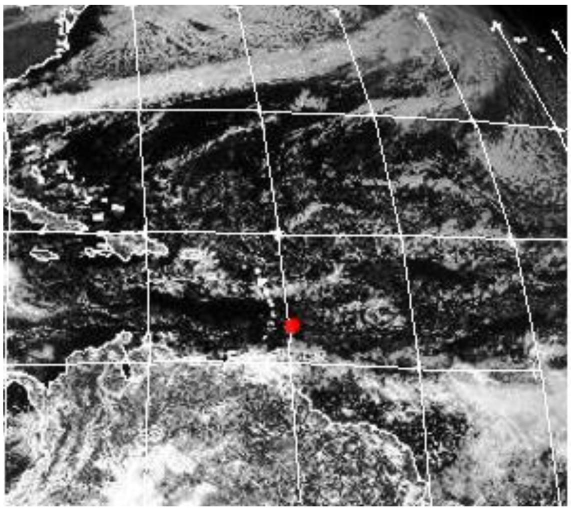

Figure 26: GEOS visible satellite image for 11 December 2013, 12 UTC.

To validate the benefit of spaceborne lidar measurements to study shallow marine convection we select NARVAL South data together with CALIPSO measurements in the same time period which were exclusively performed over the sea surfaces between -60° and -35° longitude and 10° and 20° latitude. During this campaign a number of A-Train underpasses were performed (Table 6).

Table 6: Date, time, start and endpoint of the flight, and information about CALIPSO underpasses used in this study.

Date	Time	Airport		Underpass	
		Start	End	Time	Position
10 Dec	10:14 – 20:42	EDMO	TBPB		
11 Dec	14:29 – 21:58	TBPB	TBPB	17:12 – 17:37	57.2W/14.8N – 57.9W/16.8N
12 Dec	13:50 – 20:20	TBPB	TBPB	16:21 – 16:51	43.4W/14.1N – 44.2W/17.6N
14 Dec	13:35 – 20:21	TBPB	TBPB	15:57 – 16:30	40.4W/14.3N – 41.2W/18.4N
15 Dec	15:15 – 21:45	TBPB	TBPB	16:47 – 17:16	50.7W/15.6N – 51.4W/12.2N
16 Dec	13:10 – 22:59	TBPB	EDMO	15:53 – 16:19	38.3W/19.4N – 19.4W/22.4N
19 Dec	10:05 – 19:57	EDMO	TBPB		
20 Dec	16:20 – 2:35	TBPB	EDMO	17:16 – 17:31	55.5W/13.2N – 55.9W/15.1N

For a case study we used the measurements on 11 December 2013. Figure 26 gives an exemplary overview of the situation on 11 December 2013. Small irregularly scattered clouds dominate the area over Barbados and over the Atlantic Ocean. South of about 10° N deep convective structures from the inter-tropical convergence zone (ITCZ) are present and north of about 30° N cloud structures of extra-tropical weather regimes are visible. We sampled the air masses west of Barbados in several east-west flights at different latitudes form about 18° N to about 10° N. A CALIOP underflight was performed on the flight track between 14.1° N and 57.2° W to 16.9° N and 57.8° W. The BSR cross-section of the WALES lidar and the CALIOP lidar of this about 320 km long flight track is shown in Figure 27. CALIPSO passed this flight track in less than one minute; HALO needed about 34 minutes to sample the same area.

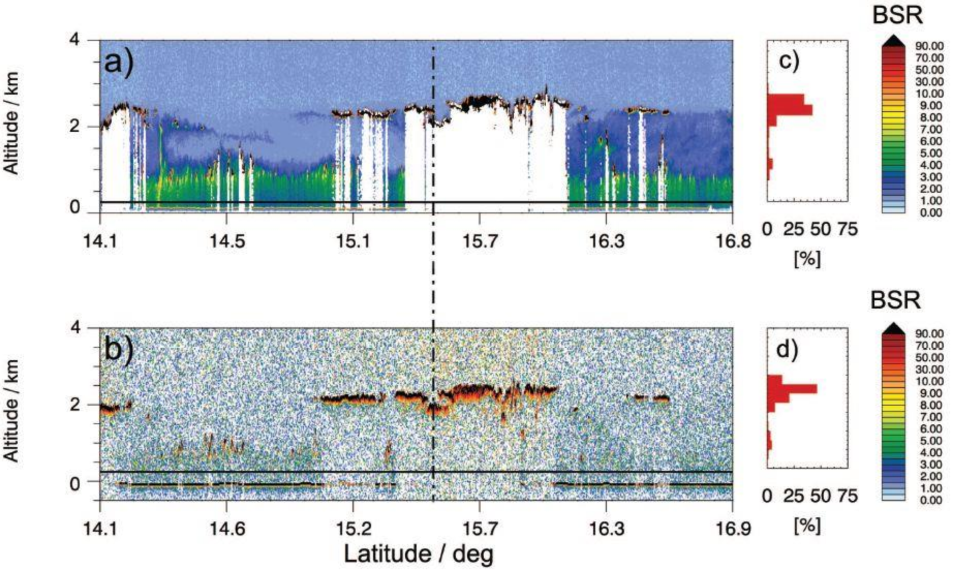

Figure 27: Backscatter ratio from (a) WALES and (b) CALIOP measurements.

Although the CALIOP measurements have a lower signal-to-noise ratio, the general aerosol and cloud structure looks the same in the WALES and the CALIOP measurements. Differences in the two measured cross-sections are mainly seen at the beginning of the underflight. Due to the different speeds of HALO and CALIOP especially highly variable cloud structures may have changed at the beginning and end of the track. Between latitudes of 15.1° N and 16.2° N the situation is dominated by a stratiform-like cloud structure with a horizontal extent of approximately 125 km. Besides this stratiform-like cloud structure small scale convective clouds with horizontal extents of less than 1 km are present at the top of the marine sub-cloud layer.

Cloud top height distribution

In a first step we compare the derived CTH distribution from space borne (CALIOP) and airborne (WALES) lidar measurements. Therefor we use all underpasses specified in Table 6. We derive the CTH independent for the CALIOP and WALES measurements and compare the derived distribution (Figure 28).

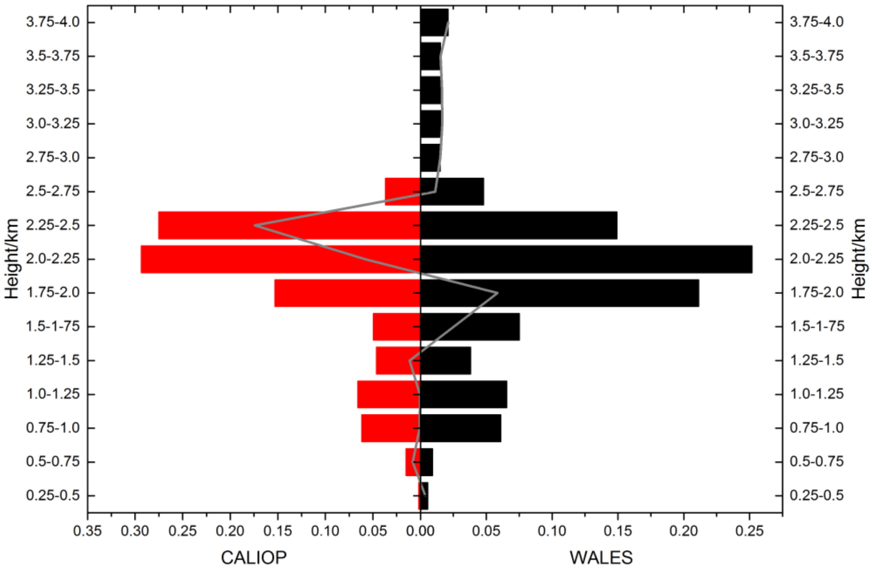

Figure 28: Cloud top height distribution derived from all CALIOP (red) and WALES (black) during all underpasses performed in the trade wind region during the NARVAL mission. The grey line shows the difference between CALIOP and WALES derived CTH fraction in each height bin.

Overall the distribution derived from WALES and CALIOP measurements show a very similar picture. Both systems show a maximum CTH between 2.0 and 2.25 km height (29% from CALIOP and 25% from WALES). And the majority of all detected clouds during the underpasses have a CTH between 1.75 and 2.5 km height (71% from CALIOP and 61% from WALES). However, in this CTH range CALIOP shows a larger fraction (27%) of the CTH in the bin between 2.25 and 2.5 km height, while the fraction of WALES derived CTHs is only 15%. In contrast, the WALES measurements determine more CTHs in the height bin between 1.75 and 2.0 km (21% in comparison to 15% derived from CALIOP measurements). Above 2.75 km CALIOP does not detect any cloud tops, while the fraction of clouds with CTH between 2.75 and 4.0 km height detected with the WALES system is about 8.5%, and thus almost compensates lower fraction of WALES derived CTHs in the height range between 1.75 and 2.5 km. Below 1.5 km height the derived CTH distribution from WALES and CALIOP agree very well with only slight differences of less than 1% in the single height bins.

Cloud length and cloud gap length distribution

In the next step we derive the cloud length and cloud gap length of the. Figure 29 shows the derived cloud length and cloud gap length distribution derived for during the underpasses from WALES 0.2 and 1 s data and from CALIOP data.

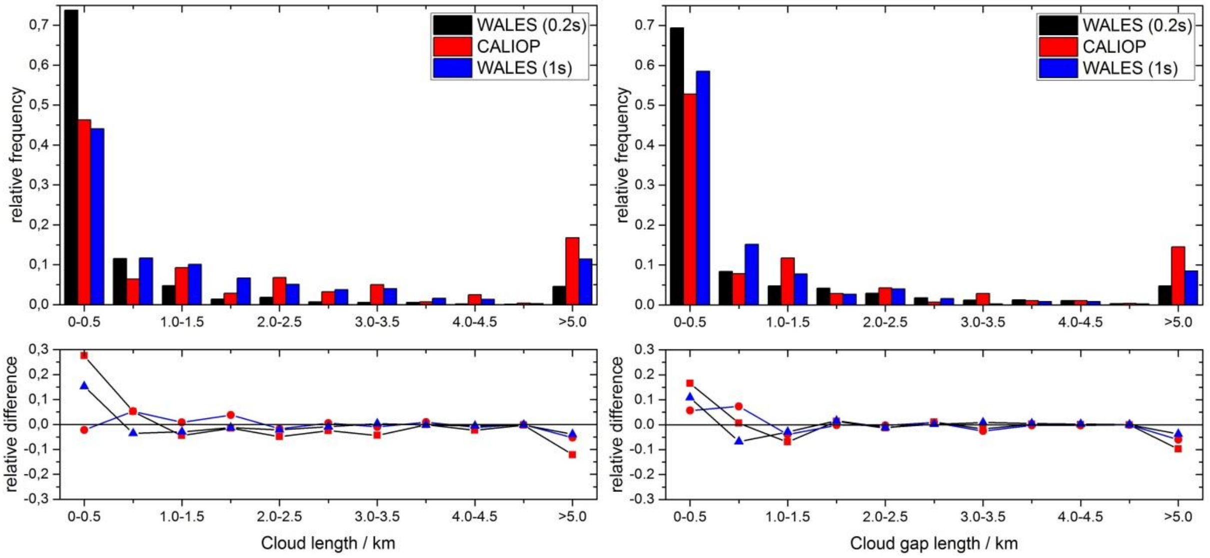

Figure 29: Cloud length (upper left) and cloud gap length (upper right) distribution in 500 m resolution derived from WALES 0.2 s data (black), CALIOP (red) and WALES 1 s data (blue) during the A-Train underpasses specified in Table 1, and differences in the contribution of the different measurements to the single range bins showing WALES 0.2 s minus CALIOP (red square), WALES 1 s minus CALIOP (red dot) and WALES 0.2 s minus WALES 1 s (blue triangle).

Comparing the 1 s resolution WALES measurements (~220 m) and the CALIOP measurements at 330 m effective resolution, one can see that the cloud length and cloud gap length distribution from both systems look quite similar. Thus the lower signal-to-noise ratio of the spaceborne measurements does not significantly affect the general quality of the satellite lidar measurements. However, comparing the high resolution WALES measurements with CALIOP and the low resolution WALES measurements, one can see quite some significant differences especially in the smallest range bin. While the contribution to cloud length of 0-0.5 m is only about 0.45 in the low resolution WALES and CALIOP measurements, it exceeds 70% in the high resolution measurements. A similar, but less significant, picture is also visible for the cloud gap length distribution. In both cases the low resolution measurements cannot resolve the finest structure of the clouds. Thus they attribute parts of the clouds to other cloud lengths and cloud gap lengths. The most prominent difference is for the high and low resolution measurements (next to the smallest length bin) is found for clouds and cloud gaps larger 5 km in extent.

Conclusion

Satellite lidar measurements are well suited to study the general situation of small scale structures. However, looking into the fine structure of these situations can lead to some deviations or biases that have to be taken into account when studying small scale structures from satellite.

5.2 Comparison of airborne and spaceborne lidar and radar measurements

To validate the performance of spaceborne lidar measurements coordinated underflights of CALIPSO and Cloudsat tracks have been done with HALO to study the different height and spatial resolution of spaceborne lidar and radar measurements. Another crucial point that should be addressed when studying the sensitivity of spaceborne measurements is the difference in retrieved results that may occur due to the different signal-to-noise ratio and resolution of airborne and satellite lidar and radar measurements. First the optimal measurement range of the single measurements on the different platforms has to be derived, and on a next step the effect of the different resolution on the derived properties has to be determined. The underflights were done during NARVAL-North as well as during NARVAL-South. For a case study we selected the measurements on 24 July 2013 over Eastern Germany during a NARVAL test flight. Figure 30 gives an exemplary overview of the situation on that day.

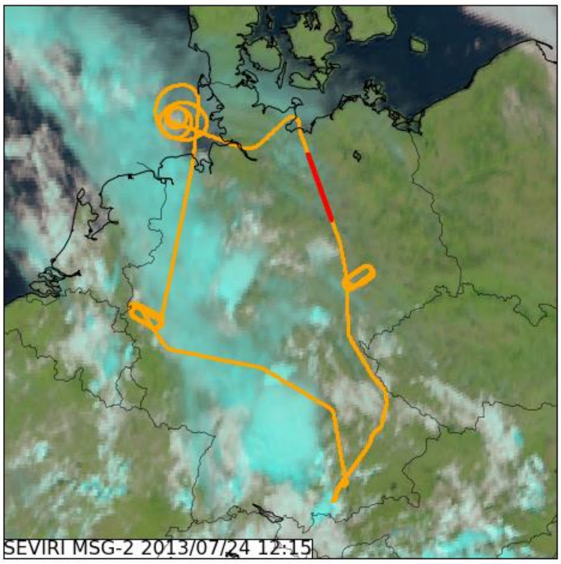

Figure 30: SEVIRI satellite image and HALO flight track for 24 July 2013. The red flight part marks the A-Train underflight.

On 24 July 2013, the mid and upper troposphere was dominated by a broad cyclonic vortex over the Eastern Atlantic and another one over Western Russia. In between of these two vortices, a weakening frontal system moved from France towards Germany and further eastwards. Ahead of this decaying cold frontal system, a quite moist airmass was advected over Germany. Along the frontal boundary, multicell storm clusters developed over the day.
The coordinated leg with CALIPSO and CloudSat featured thin, pre-frontal cirrus clouds. The satellite crossed the lag from South to North; HALO flew the satellite track in North-South

direction. Indicated by the red line in Figure 30, the underflight was performed on the flight track between 52.4° N and 11.7° E to 53.6° N and 11.3° E between 12:14 and 12:23 UTC. The backscatter coefficient cross-section of CALIOP and the radar reflectivity cross-section of CloudSat are shown in Figure 31 on the top. For comparison, the backscatter coefficient of WALES and the radar reflectivity of MIRA36 is shown in Figure 11 at the bottom. CALIPSO passed this flight track in 20 seconds while HALO needed about 9 minutes to sample the same area.

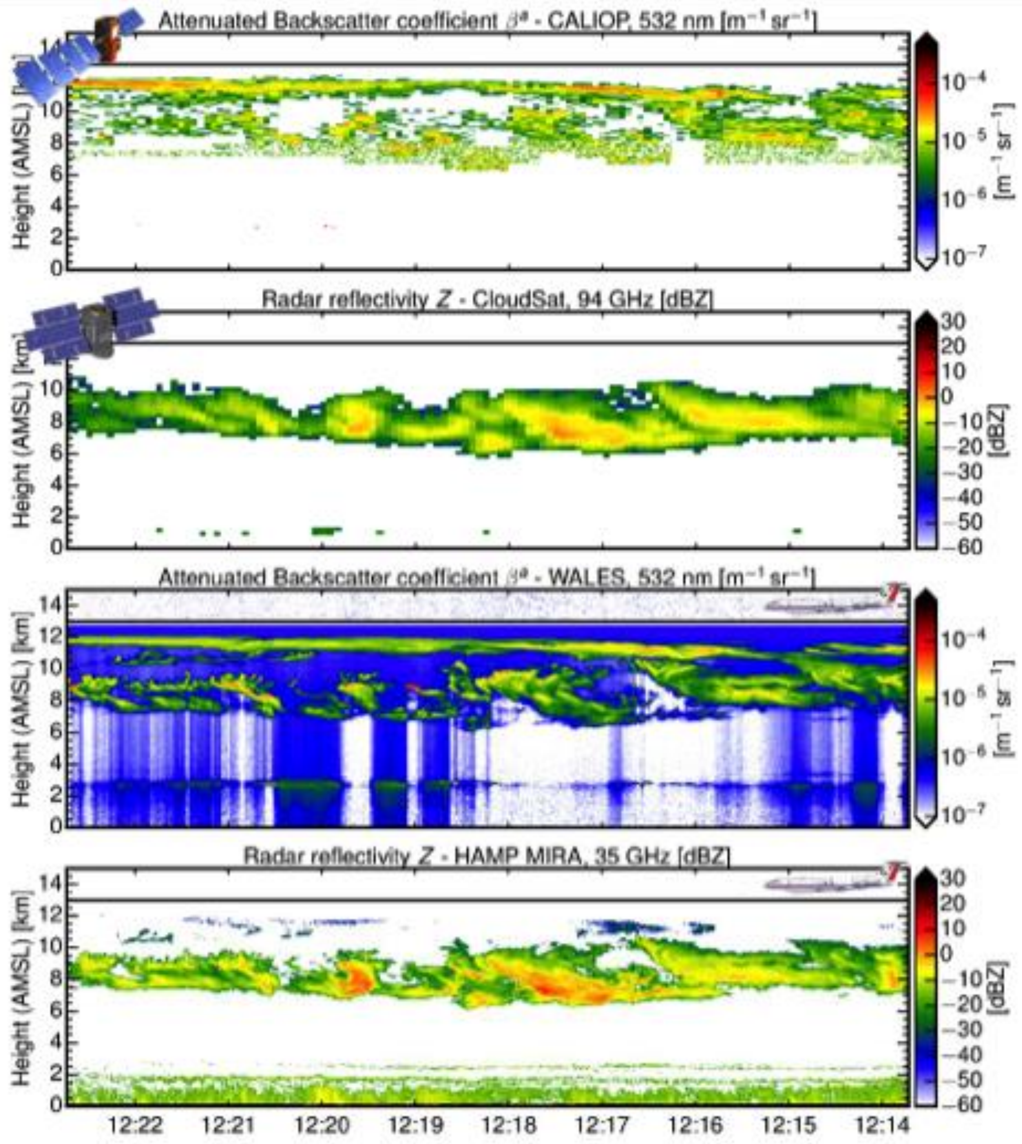

Figure 31: Lidar and radar measurements from CALIOP (uppermost panel), Cloudsat (second), WALES (third) and MIRA36 (lowest panel) during the satellite overpass marked in Figure 10.

The cirrus cloud was located in a height range from about 6 to 12 km height. Lidar measurements show a thin upper cloud layer between about 11 and 12 km height. The uppermost layer cannot be observed with the radar instruments neither from satellite nor from aircraft. The most obvious difference between the observation platforms is the coarser height and spatial resolution of the spaceborne perspective. Furthermore, highly variable cloud structures may have changed at the beginning and end of the track due to the different speeds of HALO and CALIPSO. Overall, the differences between the lidar and radar cross-sections are behaving similar for the spaceborne and airborne measurements.

Sensitivity study between airborne and spaceborne measurements

For a detailed investigation of differences in airborne and spaceborne radar and lidar measurements for this cirrus cloud case we examine the frequency distribution of the attenuated backscatter coefficient and the radar reflectivity derived from airborne and spaceborne lidar and radar measurements (Figure 32). Looking at the attenuated backscatter coefficient we see a quite good agreement between WALES and CALIOP measurements. However, values larger ~3×10^{-5} $m^{-1}sr^{-1}$ are not detected by the satellite instrument. On the other side, a larger fraction of smaller values are detected with WALES. The overall mean of the WALES measurement for this cirrus cloud case is about 2.5×10^{-6} $m^{-1}sr^{-1}$. For the CALIOP measurements we find a mean value of about 4×10^{-6} $m^{-1}sr^{-1}$.

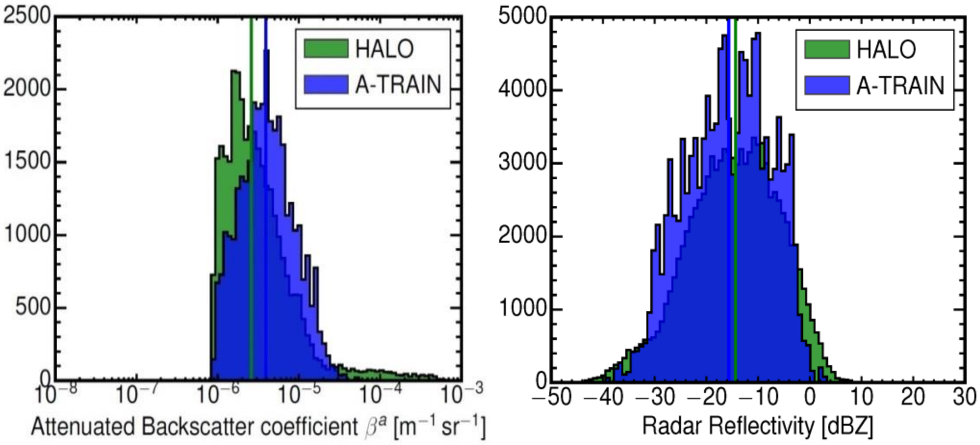

Figure 32: Absolute frequency distribution of the lidar attenuated backscatter (left) and the radar reflectivity (right) derived from WALES and MIRA36 airborne measurements on HALO (green) and from CALIOP and Cloudsat as part of the A-Train constellation (blue) for the cirrus cloud shown in Figure 31.

Besides the good agreement of the spaceborne and airborne lidar measurements also the radar measurements on both platforms show a very good agreement, although the measurements are performed at different wavelengths. The mean radar reflectivity of HALO measurements is at about -16 dBZ. The mean of Cloudsat measurements is at about -18 dBZ. Almost no values > 0 dBZ are observed from satellite measurements, while the HALO radar detects values up to about 6 dBZ. No values < -40 dBZ are detected from Cloudsat while the HALO radar detects a small fraction of values down to -44 dBZ.

Another important point when comparing airborne and spaceborne measurements is to look at the different cloud area that is seen from the same instrument type on different platforms as shown in Figure 33. Considering the lidar measurements one can see that both instruments cover most parts of the cloud. However, especially when looking at the cloud edges parts of the observed area are indicated as cloudy from the spaceborne lidar and not classified as cloud from the airborne lidar instrument. As the spaceborne lidar has a less horizontal and vertical resolution than the airborne instrument this may cause the effect that a large cloud area is defined by the spaceborne lidar. This effect is less distinct for the radar measurements at both platforms. Though the spaceborne instrument allocates some areas as cloudy while they are not classified as cloud by the airborne system these differences occur mainly at the cloud borders. On the other hand, some parts of the cloud are missed by the spaceborne system but identified by the airborne radar.

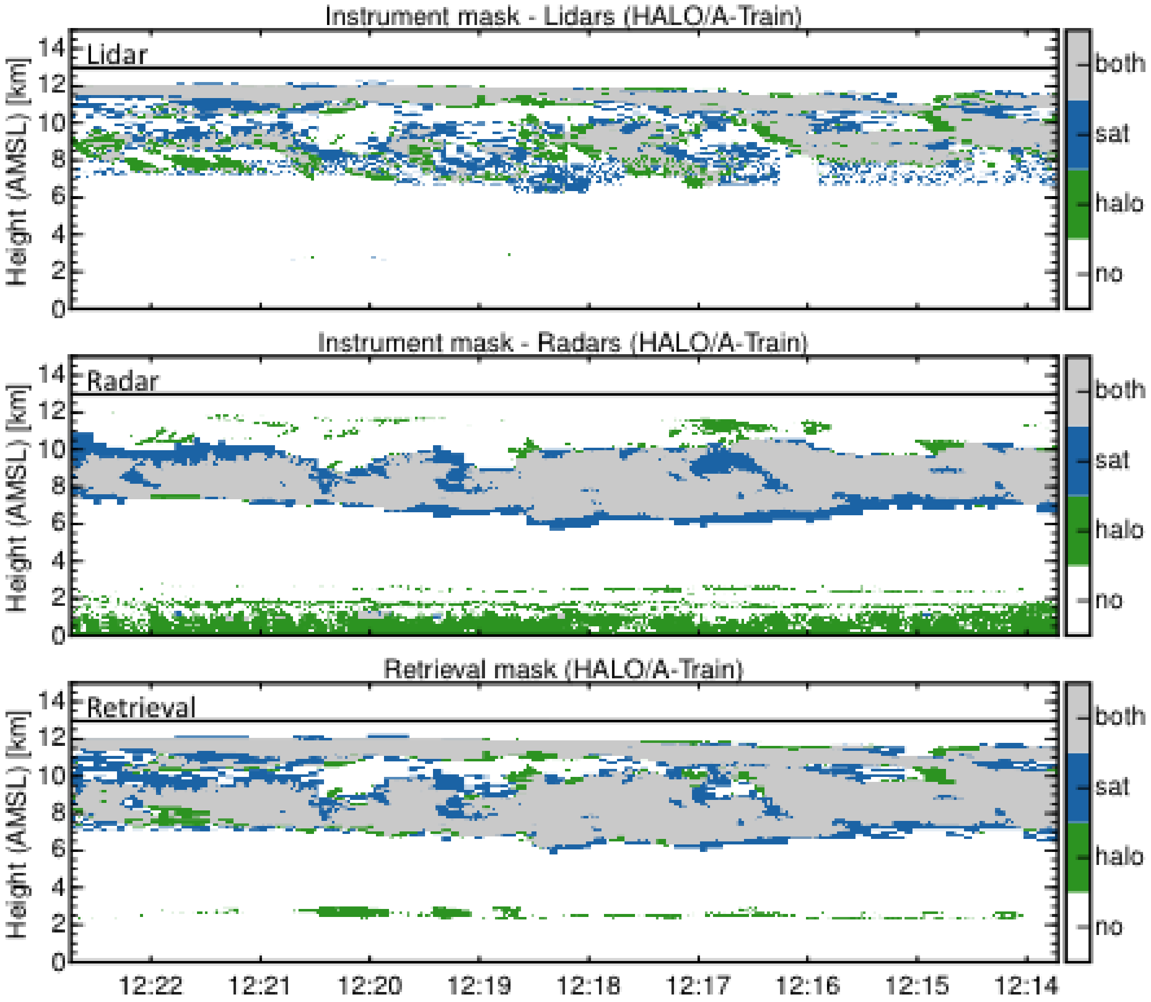

Figure 33: Instrument mask for coordinated A-Train and HALO measurements for cirrus cloud shown in Figure 31. The upper part shows the instrument mask for the CALIOP and WALES measurements, the mid-part shows the instrument mask for the Cloudsat and MIRA36 measurement, and the lower part shows the retrieval mask for combined lidar and radar measurements. Grey indicates parts where the corresponding instruments on both platforms (satellite and HALO) detect the cloud, blue indicates areas where only satellite measurements show cloud features and green indicates the areas where only HALO instruments detects cloud or aerosol features.

The differences for cloudy / cloud-free areas indicated by the different instruments on the different platforms results in a slightly different total area allocated as cloud from the different platforms. The overall cloud structure is captured quite well from the combination of lidar and radar measurements on both platforms (A-Train and HALO). However, small differences are visible. In most parts of the cloud the combined lidar and radar data from the satellite platform shows a larger cloud area, which might be caused by the lower horizontal and vertical resolution of the satellite measurements, compared to the aircraft measurements. This assumption arises from the fact, that especially at the cloud boundaries the satellite data show a larger cloud area.

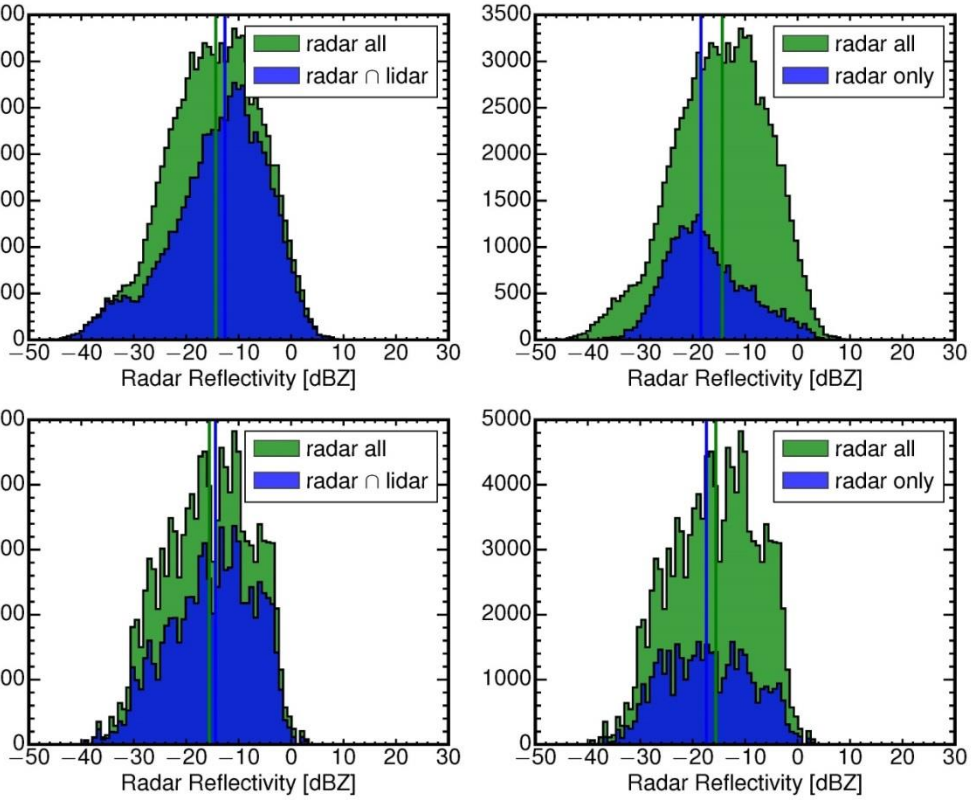

Figure 34: Absolute frequency distribution (PDF) of the radar reflectivity for the cloud scene shown in Figure 18 for HALO (uppermost plots) and Cloudsat (lowermost plots) measurements. In the left plots the PDF of the radar reflectivity of all areas inside the cloud (green) and of the radar reflectivity of the parts of the cloud with simultaneous radar and lidar measurements (blue) are shown; in the right plot the PDF of all radar measurements inside the cloud (green) and of the radar only (blue) measurements are shown.

In a next step we again investigate the different signal ranges for the parts of the cloud were both, radar and lidar, have measurements and for the part of the cloud were only one of the instruments can observe the cloud. Figure 34 shows the frequency distribution of the radar reflectivity from HALO (upper plots) and from Cloudsat (lower plots). As was already discussed in Figure 32 the overall distributions of the radar reflectivity from both platforms show some differences. Looking now on the part of the cloud, which can be observed by radar and lidar and on those, observed only by radar we find some common structures. Both platforms show that the intersection of radar and lidar shows larger values of the radar reflectivity; though this is more pronounced from radar measurements on HALO. While Cloudsat measurements show only a small difference of the mean radar reflectivity of about -11 dBZ for the intersection and of about -12 dBZ in the radar only areas, this difference is more distinct for the HALO radar measurements; showing a mean radar reflectivity of about -11 dBZ for the intersection and of about -20 dBZ for the radar only areas. In this cirrus case almost all values < -20 dBZ for HALO measurements showed radar only measurements while even at the highest values both, radar and lidar measurements from HALO observed the cloud. This is slightly different to the cirrus cloud case discussed in Section 4. It is also not visible from the Cloudsat measurement where we found similar behaviour as in Section 4.

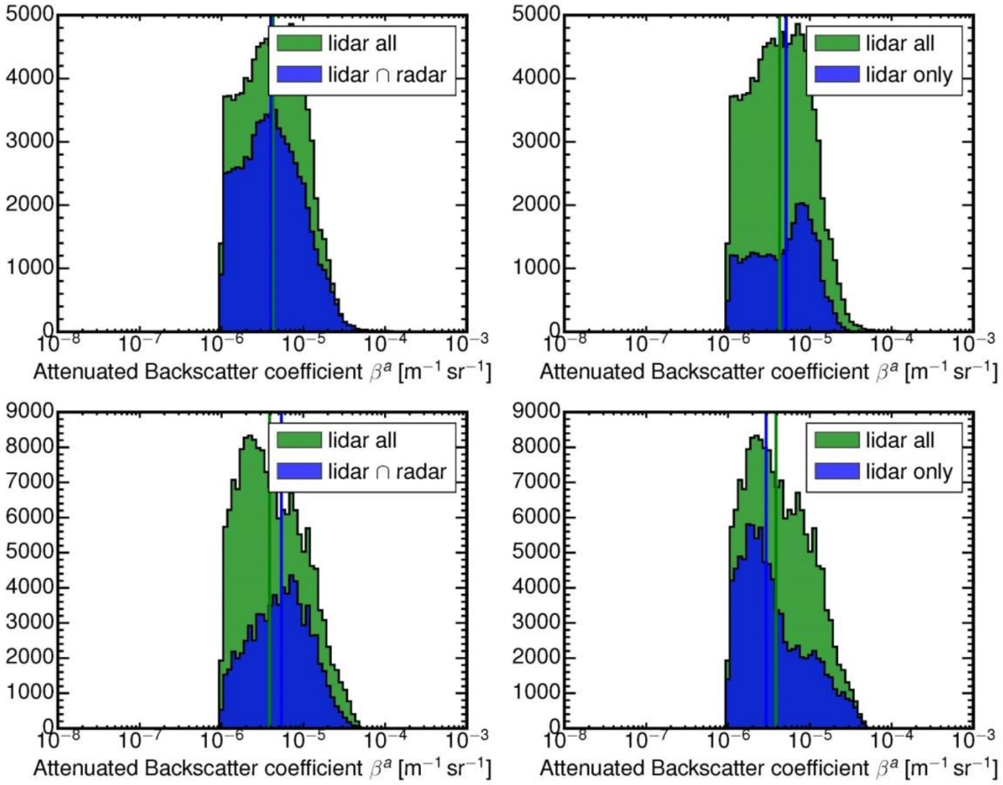

Figure 35: Absolute frequency distribution (PDF) of the attenuated backscatter coefficient for the cloud scene shown in Figure 18 for HALO (uppermost plots) and CALIOP (lowermost plots) measurements. In the left plots the PDF of the lidar attenuated backscatter coefficient of all areas inside the cloud (green) and of the lidar attenuated backscatter coefficient of the parts of the cloud with simultaneous radar and lidar measurements (blue) are shown; in the right plot the PDF of all lidar measurements inside the cloud (green) and of the lidar only (blue) measurements are shown.

Looking at the lidar measurements from CALIOP and HALO (Figure 35) we see a similar behaviour as discussed in Section 4. The total value range for the attenuated backscatter coefficient is about 1x10^{-6} $m^{-1}sr^{-1}$ to 5x10^{-4} $m^{-1}sr^{-1}$ for the HALO lidar measurements and about 1x10^{-6} $m^{-1}sr^{-1}$ to 3x10^{-5} $m^{-1}sr^{-1}$ for the CALIOP measurements. Thus the attenuated backscatter coefficient range of this cirrus cloud case covers smaller values than the one shown in Section 4. This is reflected in the mean attenuated backscatter coefficient of this cirrus cloud of about 2.5x10^{-6} $m^{-1}sr^{-1}$ independent from the platform compared to the mean value of about 1x10^{-5} $m^{-1}sr^{-1}$ in the former case. Considering now the parts of the cloud with both, lidar and radar measurements, and of the part of the cloud with only lidar measurements we see some similar behaviour as in the former case. From both platforms most parts of the cloud are observed by lidar and radar. Only a small fraction is observed by lidar only. The value range of this lidar only parts is in the lower part of the overall value range of the attenuated backscatter ratio. However, the mean value of the lidar only part and the overall mean value show only small differences compared to the former case, and the lidar only part does not exclusively cover the lower value range of the attenuated backscatter coefficient distribution. A significant fraction of radar and lidar measurements was found down to an attenuated backscatter coefficient of about 1x10^{-6} $m^{-1}sr^{-1}$.

Influence of different sensitivity and different retrieval versions

The radar and lidar measurements shown in Figure 31 are used to retrieve the ice water content (IWC) and the effective radius (REFF) applying the synergistic analysis retrieval described in Section 4. As already seen for the lidar and radar measurements also the retrieved IWC and REFF (Figure 36) retrieved from airborne measurements show better resolution compared to the same properties retrieved from spaceborne measurements; depicting the fine structure of the cloud.

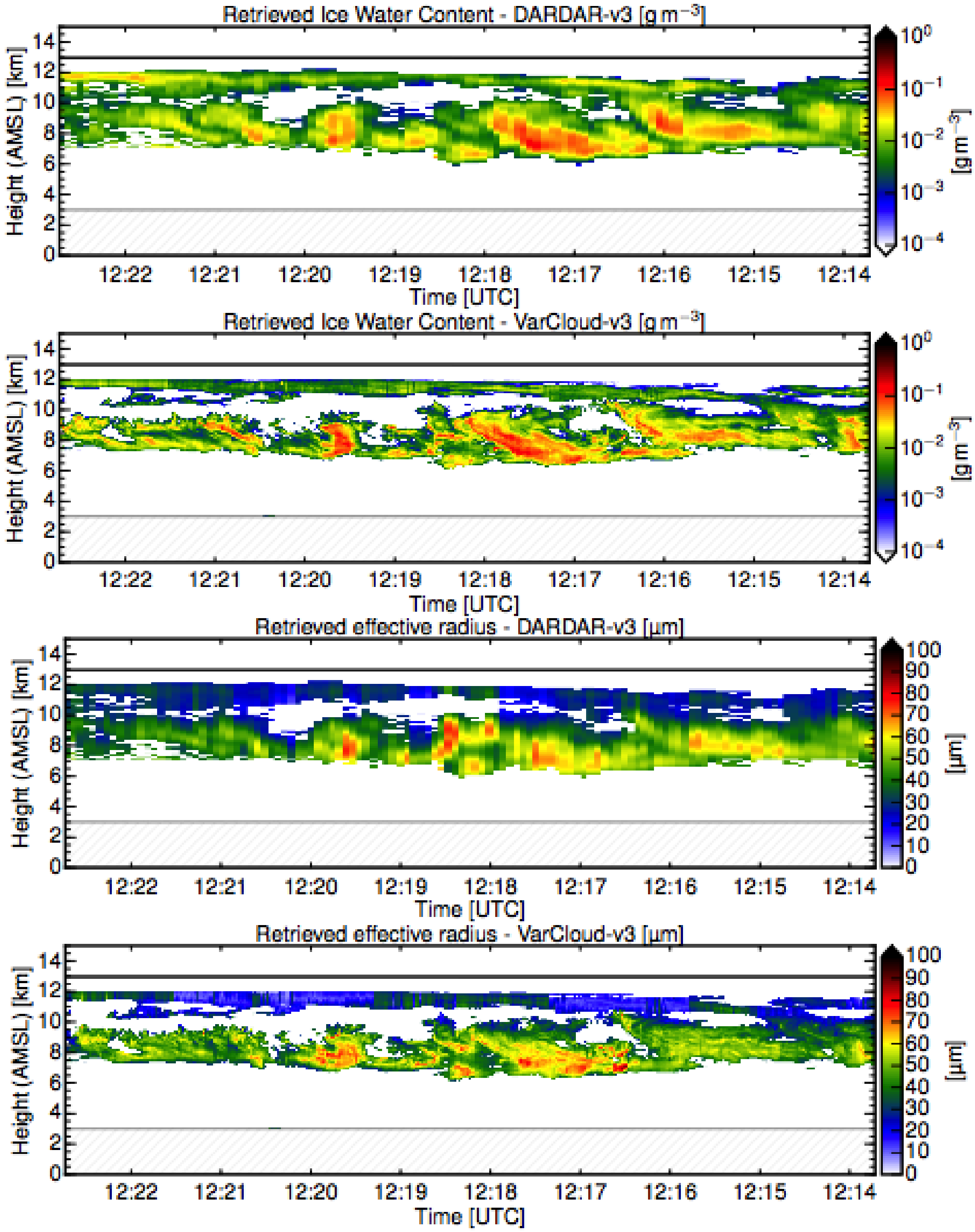

Figure 36: Retrieved ice water content and effective radius from HALO and A-Train lidar and radar measurements for the cirrus cloud case shown in Figure 31.

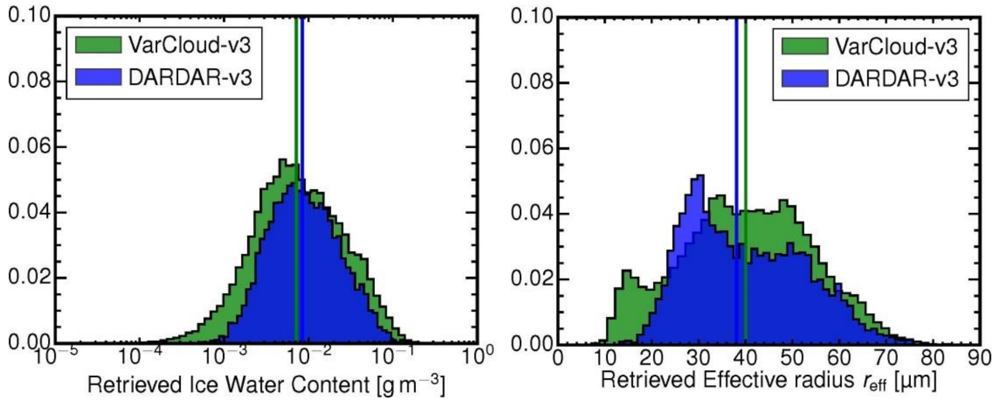

Figure 37: Relative frequency distribution of the retrieved ice water content and effective radius from radar and lidar measurements on HALO and A-Train as shown in Figure 36.

From the frequency distribution of the retrieved IWC and REFF from both platforms (Figure 37) we see the good agreement in the retrieved properties applying the same algorithm on airborne and spaceborne measurements. HALO measurements show only a slightly broader value range for the IWC than spaceborne measurements but the overall IWC mean value for both platforms of about 8x10^{-3} gm^{-3} agrees well. The overall value range for the retrieved IWC is between about 1x10^{-3} and about 1x10^{-1}. Also for the retrieved REFF the same overall mean value of 38 µm is found from airborne and spaceborne measurements. However, compared to the IWC distribution we find a clearly broader value range for the REFF retrieved from airborne measurements compared to spaceborne measurements. The REFF distribution derived from the HALO measurements shows a larger fraction of smaller values (10 – 20 µm) compared to the REFF distribution of the CALIOP/Cloudsat measurements were almost no REFF values < 20 µm are found. Also a slightly larger fraction of larger values with REFF > 70 µm are found from HALO measurements. The REFF distribution from measurements on both platforms shows a two modal structure with a first maximum at about 30 µm and a second maximum at about 50 µm. From Figure 36 one can see that the large REFF values are mainly found in the lower part of the cloud.

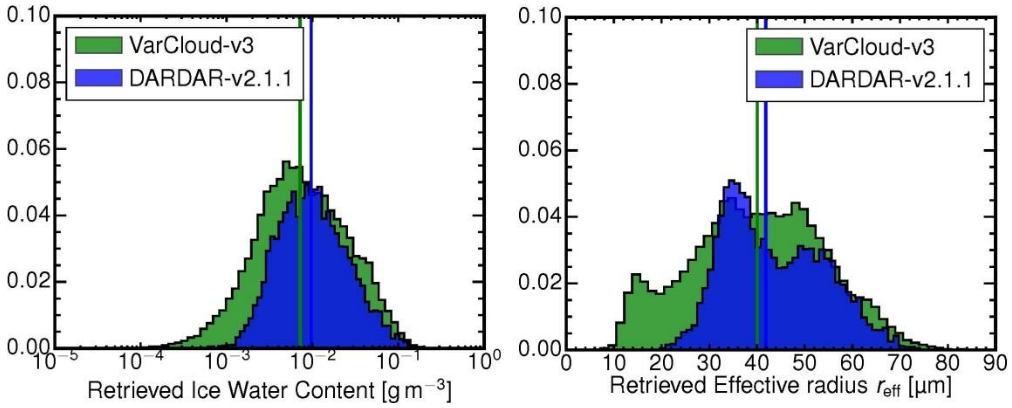

Figure 38: Relative frequency distribution of the retrieved ice water content and effective radius from radar and lidar measurements on HALO and A-Train (DARDAR version) as shown in Figure 36.

For the comparison shown in Figure 37 we applied the same synergistic analysis retrieval on the measurements of both platforms. The comparison is now done using the same version of the synergistic algorithm for the aircraft data but the operational DARDAR version for the spaceborne data (Figure 38). Both retrievals mainly differ in slightly different a-priori information with respect to lidar ratio and size distribution. Although the differences in the retrieved IWC are little, one can see for both, the IWC and the REFF, a slight shift or shortening towards higher values. For the IWC distribution the mean value is shifted to 1x10^{-2} gm^{-3}. For REFF the differences are a bit more distinct: The mean value is shifted from 38 µm to 42 µm, and the first maximum of REFF is shifted from values of about 25-30 µm to values of about 30-35 µm. Additionally the second maximum is more pronounced using the DARDAR version moving from around 50 µm to about 50-60 µm.

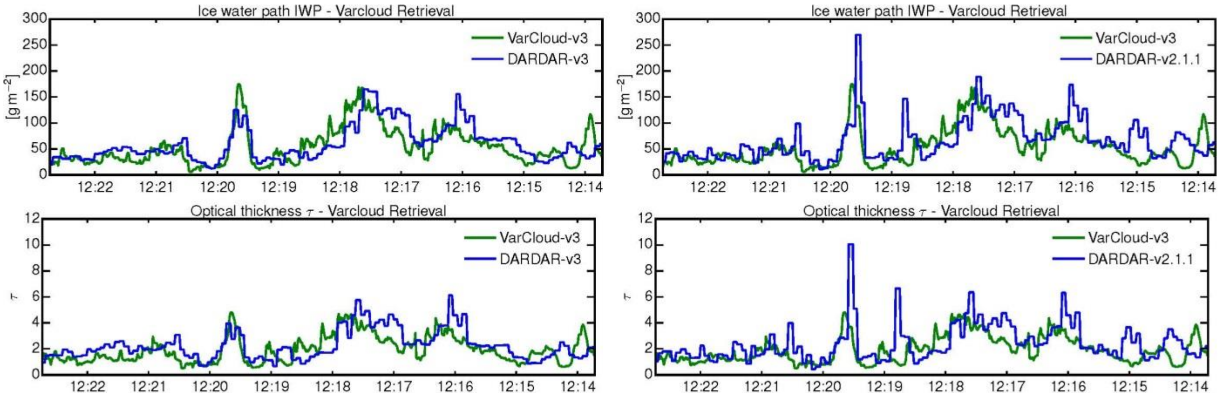

Figure 39: Retrieved ice water path (upper plot) and optical thickness (lower plot) derived from HALO and A-Train measurements as shown in Figure 31. The left plots compare the IWP and OD using the same version of the algorithm; for the right plots the operational DARDAR algorithm is used for CALIPSO and Cloudsat measurements.

In a next step we compare the integrated properties (IWP and OD) along the flight track and look how the use of different versions of the algorithm affects these properties. Figure 39 shows that the IWP and the OD of the cloud derived from airborne and spaceborne measurements in principle agree very well. Small differences are visible with respect to the resolution of the data. Comparing furthermore the integrated properties calculated with different versions of the algorithm, as it is the case for the A-Train measurements, one can see additional small differences; e.g. the peaks in IWP and OD are partly better captured using the DARDAR version.

Conclusion

Combining airborne and spaceborne measurements the latter are much more effected by noise and coarser resolution. However in principle they show a good agreement. Looking at the comparison of different versions of synergistic analysis retrievals one can see, that the results show partly large differences, resulting from different input parameters or feature masks. Further investigation of these effects would be very valuable.

6. EFFECTS OF USED RADAR WAVELENGTHS

6.1 Model study of radar reflectivity at 35 GHz and 95 GHz

In this study, the influence of radar wavelength on radar reflectivity will be analyzed on the basis of numerical models. Due to the strong dependence of radar reflectivity on ice crystal size, a realistic and well tested distribution of ice crystal sizes is crucial. Since particle size distributions (PSD) are known to be highly variable (Intrieri et al., 1993), we chose the normalized PSD approach by Delanoe et. al. (2005) which is based on an extensive database of airborne in situ microphysical measurements. Furthermore, this PSD is a central component of the already introduced synergistic radar-lidar retrieval and thus integrates seamlessly into the previous studies. **Figure 40** shows multiple normalized PSDs as a function of mean melted diameter D_{eq} for different effective ice crystal radii.

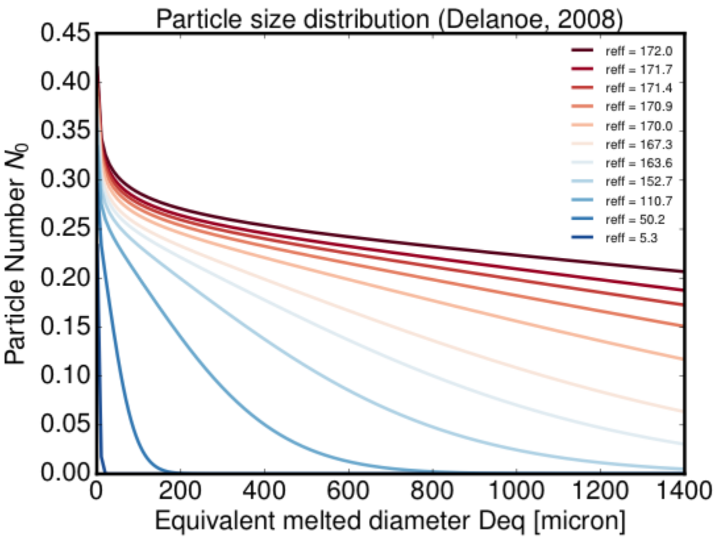

Figure 40: Normalized partical size distribution used during the radar reflecitivy study. The distribution was taken from Delanoe (2005) and is a central component of the already introduced synergistic radar-lidar retrieval. It is based on an extensive database of airborne in situ microphysical measurements.

The ice crystal shape and the electromagnetic scattering properties are another important assumption. In the following, 'Rayleigh scattering only' will be compared to Mie scattering and T-Matrix scattering theory. In the case of Mie scattering, area-size and mass-size relationships are taken from Francis et al. (1998) and Brown and Francis et al. (1995) respectively. Mie theory is applied assuming homogeneous ice-air spheres, while the T-Matrix calculations are done for spheroids with an aspect ratio of 0.6 and same mass and area like the ice-air spheres.

The model results for a single ice crystal are shown in the left panel of **Figure 41**. Here, the radar reflectivity at 35 GHz (green) and 95 GHz (red) is shown as a function of equivalent melted ice crystal diameter D_{eq} according to Rayleigh (blue), Mie (drawn) and T-Matrix (dashed) theory. While the radar reflectivity derived with Rayleigh theory steadily increases with particle size to the power of six, the values start to deviate for Mie and T-Matrix theory at a D_{eq} of around 400 µm at 95 GHz and around 800 µm at 35 Ghz. At D_{eq} larger than 600 µm (1200 µm), radar reflectivity for single ice particles even decreases again at 95 GHz (resp. 35 Ghz) due to Mie resonances. In a next step, this result is convolved with the normalized PSDs with different effective radii. The results for a fixed ice crystal concentration of N = 10^6 crystals per cubic meter and variable effective ice crystal radius is shown in the right panel of **Figure 41**.

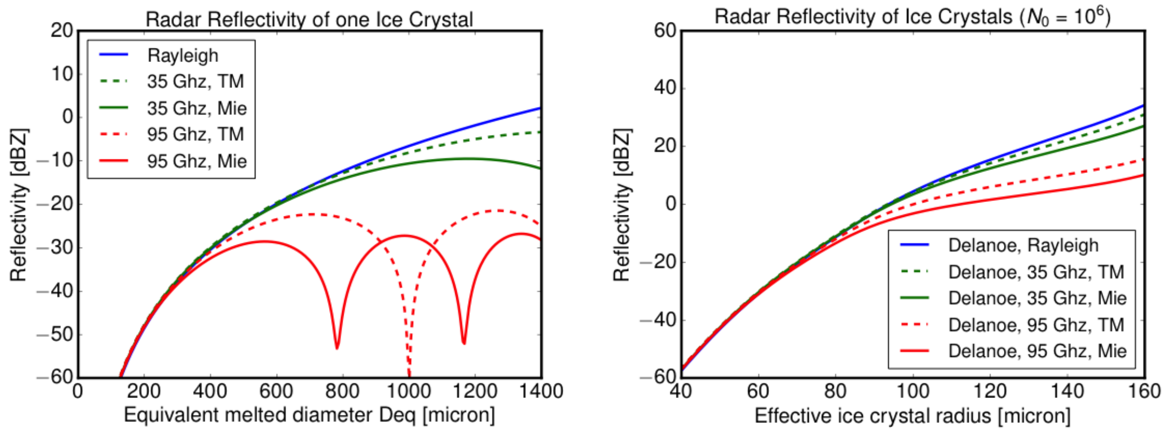

Figure 41: Modeled radar reflectivities at 35 GHz (green) and 95 GHz (red) as a function of equivalent melted ice crystal diameter Deq according to Rayleigh (blue), Mie (drawn) and T-Matrix (dashed) theory. While the left panel shows results for monodisperse ice crystals, the right panel shows results for N = 106 crystals distributed according the PSD in Fig. 34.

Again, lower radar reflectivity values are almost identical, while larger radar reflectivities at 95 GHz are below the values at 35 GHz. For these realistic PSDs, radar reflectivities deviate from Rayleigh theory for effective radii larger than 80 µm at 95 GHz and 120 µm at 35 GHz. Thus, the radar reflectivity of realistic PSDs deviates at much smaller effective radii when compared to the study of single ice crystals. This is caused by a few but large ice crystals contained in each PSD, which dominate the radar reflectivity. Furthermore, the results obtained from Mie and Rayleigh theory can be thought as theoretical boundaries for more complex shaped particles.

In a last study, this is used to confine the values of possible radar reflectivities when measurements at 95 GHz are compared to co-located measurements at 35 GHz. In **Figure 42** modeled radar reflectivity from **Figure 41** at 95 GHz is plotted against reflectivity at 35 GHz. Again, the blue lines show the Rayleigh result, the drawn lines show result according to Mie theory and the dashed lines show results for spheroids which were obtained from T-Matrix theory. In Figure 42 on the left, result are again shown for monodisperse ice crystals of different sizes, while the right panel shows results for N = 10^6 crystals distributed according the normalized PSDs.

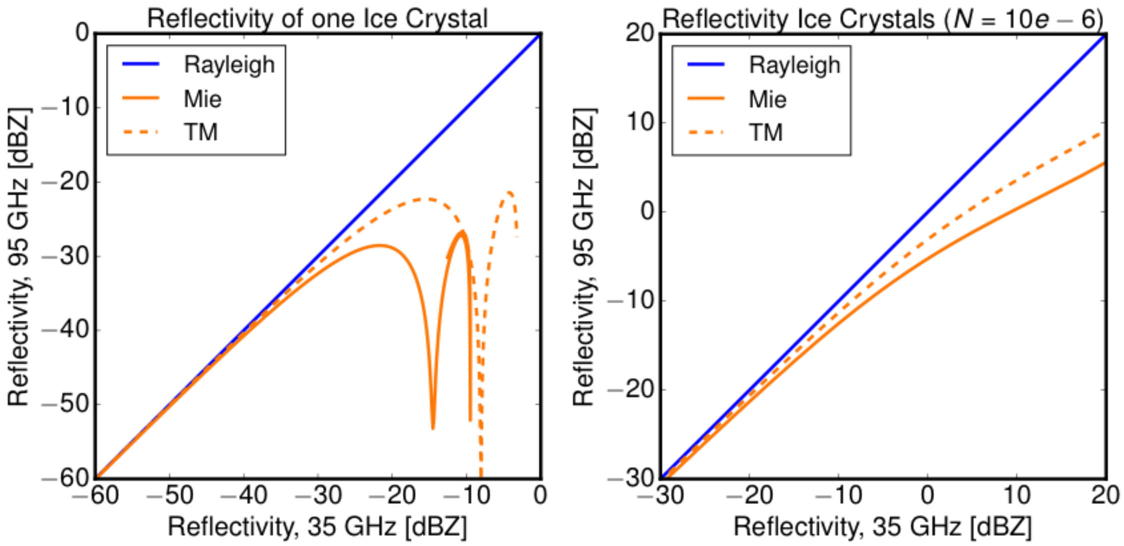

Figure 42: Comparison between modelled radar reflectivities (shown in Figure 34) at 95 GHz against radar reflectivities at 35 GHz according to Rayleigh (blue), Mie (drawn) and T-Matrix (dashed) theory. Like in Figure 34, the left panel shows results for mono-disperse ice crystals, while the right panel shows results for N = 106 crystals distributed according the PSD in Figure 34. Overall, lower radar reflectivity values are almost identical, while larger radar reflectivities at 95 GHz are below the values at 35 GHz.

6.2 Airborne radar measurements at different wavelengths

A critical point for the validation of future EarthCARE measurements is the adaptability of measurements at different wavelength and their impact on the retrieved results. To study this, a coordinated flight with the French Falcon equipped with the 95 GHz radar system RASTA (Radar system airborne) was performed on the transfer flight to Barbados over Southern France and Northern Spain on 19 December 2013.

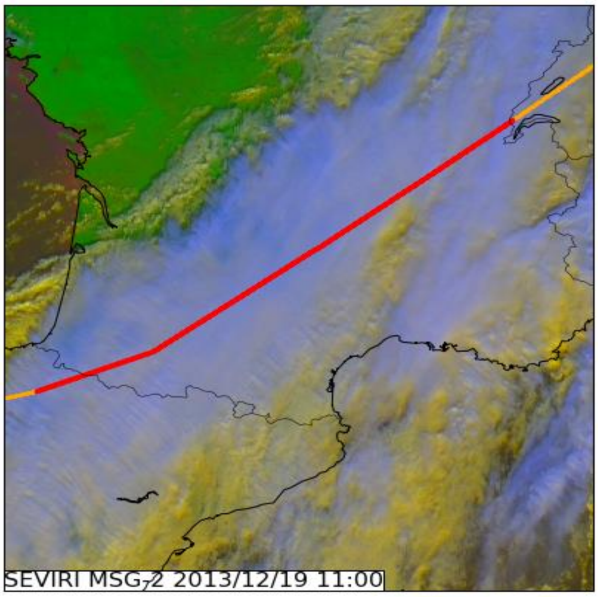

Figure 43: SEVIRI satellite image and HALO flight track for 19 December 2013. The red flight part marks the coordinated flight leg with the French Falcon and the 95 GHz airborne lidar RASTA.

The measurement area was influenced by clouds, which reached up to about 10 km in altitude. Thus this coordinated flight provides an optimal measurement situation for a radar intercomparison. Figure 43 shows a satellite image (HRV-RGB) from SEVIRI (Spinning enhanced visible and infrared imager) at 11:00 UTC with the corresponding flight track of HALO in orange and the common flight leg with the French Falcon in red.

For the period between 11:00 UTC and 11:15 UTC, both aircraft flew in close separation of less than 5 minutes. During that leg, HALO was flying at an altitude of 13 km and passed the slower flying French FALCON at an altitude of 10 km. For this section along the coordinated flight track marked in Figure 43, Figure 44 shows radar measurements performed with the MIRA 36 at 36 GHz (upper panel) and the RASTA system at 95 GHz (lower panel). In both instrument measurements, the cirrus cloud layer between 6 and 10 km as well as the lower precipitating clouds and the ground return are clearly visible. Due to the close separation of the aircrafts, many cloud features can be found in both measurements at the same place.

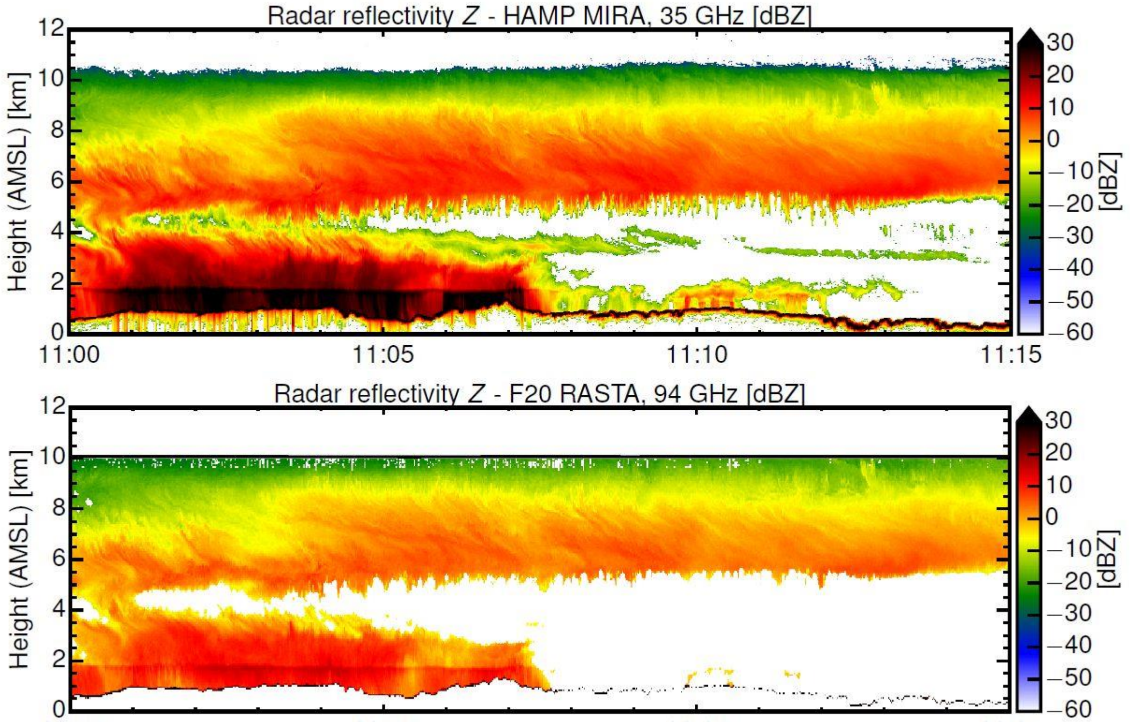

Figure 44: Radar measurements performed with the MIRA 36 at 36 GHz (upper panel) and the RASTA system at 95 GHz (lower panel) along the coordinated flight track marked in Figure 30.

In the most western part of the flight, low clouds up to about 4 km are visible, which are topped by a cloud layer from about 6 to 10 km height. This uppermost cloud layer is visible during the whole coordinated flight. In the eastern part of the flight track further low clouds occur with signals of rain beneath about 1-1.5 km height. On the first sight of the measurements one can suggest that the MIRA36 system shows more variability within the cloud layer. Also small-scale cloud structures are visible in the measurements from about 1° to 3° E. These cloud structures are not visible in the cross-section of the RASTA measurements. At first glance, the MIRA 36 at 36 GHz is more sensitive, especially to low-lying water clouds.

While the radar reflectivity of the high cirrus cloud layer is quite similar, differences become visible in precipitating clouds.

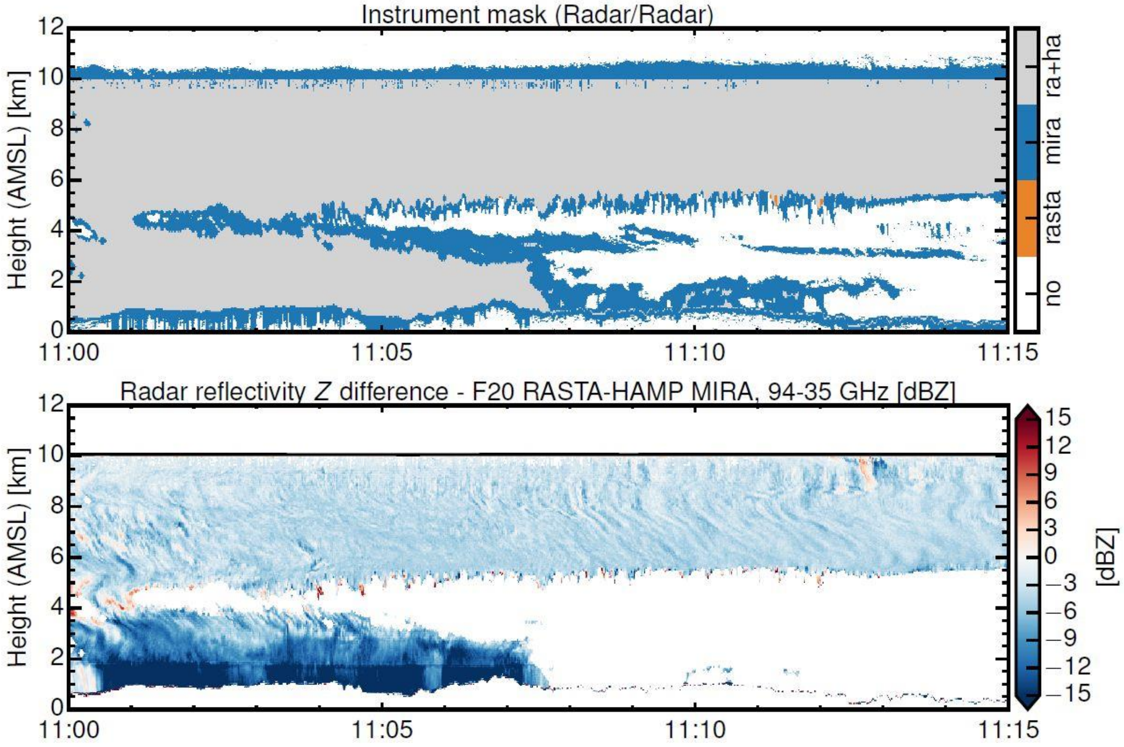

Figure 45: (top) Instrument mask for the common radar measurements shown in Figure 31. Grey indicates parts where both platforms (MIRA 36 and RASTA) detect a cloud, blue indicates areas where only MIRA detects clouds and red indicates the areas where only RASTA detects clouds. (bottom) Radar reflectivity differences between the RASTA and MIRA measurements.

The different sensitivity and radar reflectivity is analyzed in more detail in Figure 45. The top panel in Figure 45 shows an instrument mask for the common radar measurements. In this figure, grey indicates parts where both platforms (MIRA 36 and RASTA) detect a cloud, blue indicates areas where only MIRA detects clouds and red indicates the areas where only RASTA detects clouds. As already mentioned, the MIRA 36 is clearly more sensitive to low-lying water clouds. This is not only valid for the precipitating clouds between 11:00 - 11:05 UTC, but also for the non-precipitating water clouds after 11:07 UTC. The system is also more sensitive to cirrus cloud edges, which is visible at the base of the cirrus cloud layer. It can be concluded, that the 35 GHz system is more sensitive in regions with very few but large cloud crystals (cirrus cloud base) and simultaneously in regions with many but small cloud droplets (low-lying water clouds). Here, the considerable higher pulse peak power (30 kW vs. 1.8 kW), the larger antenna diameter (100 cm vs. 30 cm) and the lower attenuation plays in favor of the 35 GHz system. This demonstrates how system parameters can compensate the considerably smaller backscatter efficiency at 35 GHz. In Figure 45 on the bottom, radar reflectivity differences are shown between the RASTA and MIRA measurements. As already mentioned, the radar reflectivity is quite similar in the cirrus cloud layer with slightly smaller values at 95 GHz. This difference becomes more and more pronounced towards lower altitudes with precipitating clouds. As discussed in the previous model study, this difference can be explained with the difference in radar wavelengths. With larger particle size, the electromagnetic scattering is leaving the Rayleigh regime (D << λ) towards the Mie regime (D >> λ) at much smaller particle sizes at 95 GHz compared to 35 GHz. Furthermore, the difference between 95 and 35 GHz increases with radar reflectivity.

This observation is in good agreement with the results of the preceding model study. This is illustrated in **Figure 46**. The comparison of modeled radar reflectivities at 35 GHz and 95 GHz on the left panel is put into contrast with the comparison of measured radar reflectivities at the two wavelengths on the right panel. In both cases, radar reflectivity values are almost identical at lower values, while the radar reflectivity difference between 95 GHz and 35 GHz increases with increasing radar reflectivity. Here, the measured reflectivities remain well within the possible region between Rayleigh and Mie regime shown on the left in Figure 46. Most values are above the theoretical Mie results, which indicate the presence of non-spherical particles.

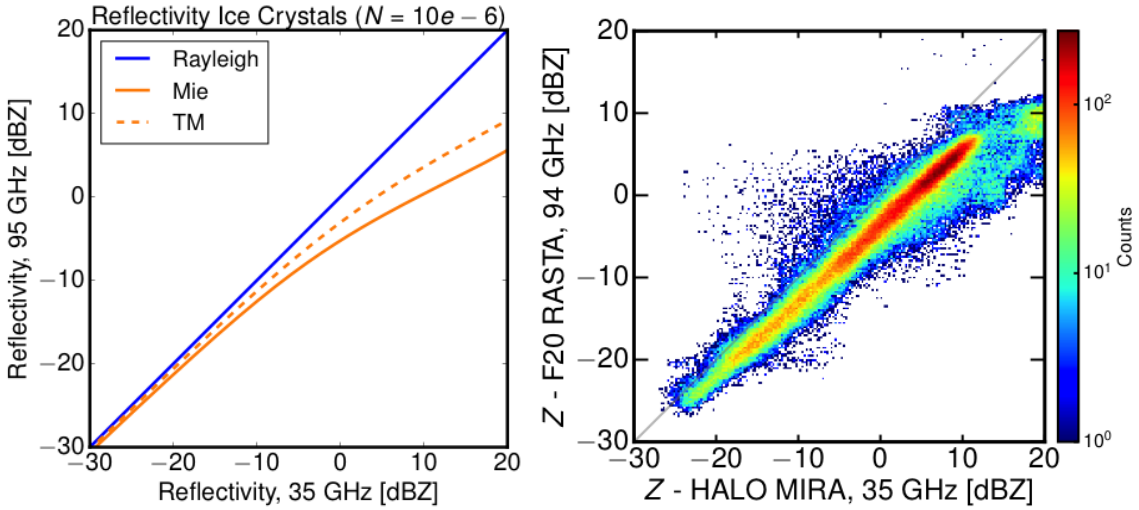

Figure 46: Comparison between radar measurements shown in Figure 31 performed with the MIRA at 35 GHz and the RASTA system at 95 GHz. While lower radar reflectivity values are almost identical between both wavelengths, larger radar reflectivities at 95 GHz are below the values at 35 GHz. This is in good agreement with simulated reflectivities shown in Figure 35 (right).

Conclusion

The higher sensitivity as well as the lower attenuation of the 35 GHz MIRA can be seen as a useful supplement to the existing 95 GHz RASTA. For joint flight legs, the 35 GHz system can serve as a standard to validate the sensitivity of an air- or space-borne 95 GHz system. Moreover, the common measurements can be used to check the attenuation correction of L2 processors and the correct handling of different radar wavelengths.

7. EFFECT OF USED LASER WAVELENGTH (literature study)

8.1 Aerosol classification

It is common knowledge, that the intensive optical properties measured by lidar (i.e. the lidar ratio and the particle linear depolarization ratio) are quite different for different aerosol types and thus appropriate for aerosol typing (Burton et al., 2012; Groß et al., 2013, 2015a). These optical properties were measured with similar lidar systems (i.e. EARLINET quality assured lidar systems) during different measurement campaigns. Measurements at 355 nm were performed with the ground-based Raman polarization lidars POLIS of the Ludwig-Maximilians-Universität München (Groß et al., 2011) and with PollyXT (Engelmann et al., 2016) of the Leibniz Institute for Tropospheric Research Leipzig. Measurements were conducted during SALTRACE at Barbados (Groß et al., 2015b), during SAMUM-2 in Cape Verde (Groß et al., 2011), in the framework of EARLINET in Leipzig and Munich (Illingworth et al., 2015; Wiegner et al., 2011; Groß et al., 2012) and in the Amazon Basin (Baars et al., 2012) Thus the intensive optical properties of different types of aerosols could be studied and compared. Figure 47 gives an overview of simultaneously performed measurements of both properties for different aerosol types.

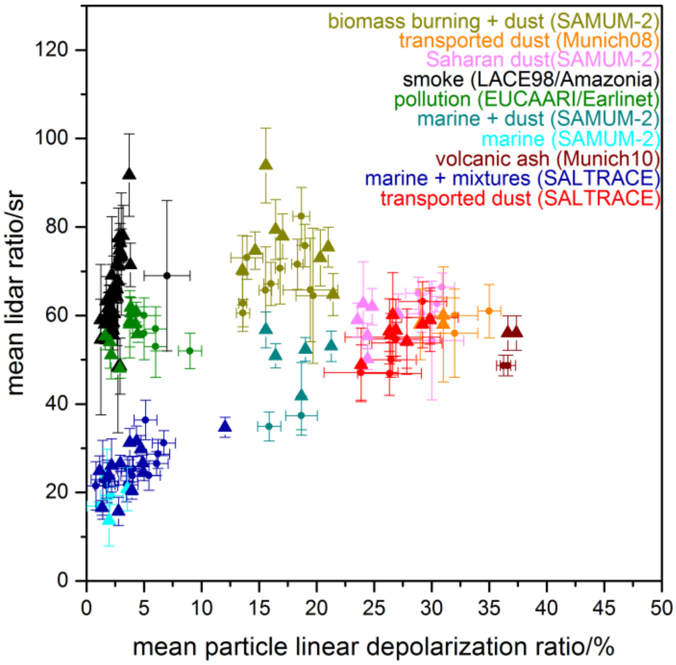

Figure 47: Aerosol classification at 355 (triangles) and 532 nm (circles) based on the lidar ratio and the particle linear depolarization ratio. Measurements at 355 nm were performed with the ground-based Raman polarization lidars POLIS of the Ludwig-Maximilians-Universität München (Groß et al., 2011) and with PollyXT (Engelmann et al., 2016) of the Leibniz Institute for Tropospheric Research Leipzig. Measurements were conducted during SALTRACE at Barbados (Groß et al., 2015b), during SAMUM-2 in Cape Verde (Groß et al., 2011), in the framework of EARLINET in Leipzig and Munich (Illingworth et al., 2015; Wiegner et al., 2011; Groß et al., 2012) and in the Amazon Basin (Baars et al., 2012). Figure adapted from Groß et al, 2015b.

One can see that the different aerosols show quite different clusters of in the lidar ratio and particle linear depolarization ratio space. These differences in the combined optical properties are more distinct for the different aerosol types as for the different wavelengths; considering measurements at 355 nm and at 532 nm. Looking at the mean values of the particle linear depolarization ratio and the lidar ratio at 355 and 532 nm shown in Figure 47 one can see, that for the majority of the aerosol types the intensive optical properties are quite similar within the uncertainty range (Figure 48). Only smoke and Saharan dust (before its long-range transport) show small differences in the retrieved intensive optical properties. This mainly affects aerosol typing based on these lidar properties and requires slightly modified values for the aerosol classification thresholds (Groß et al., 2015a).

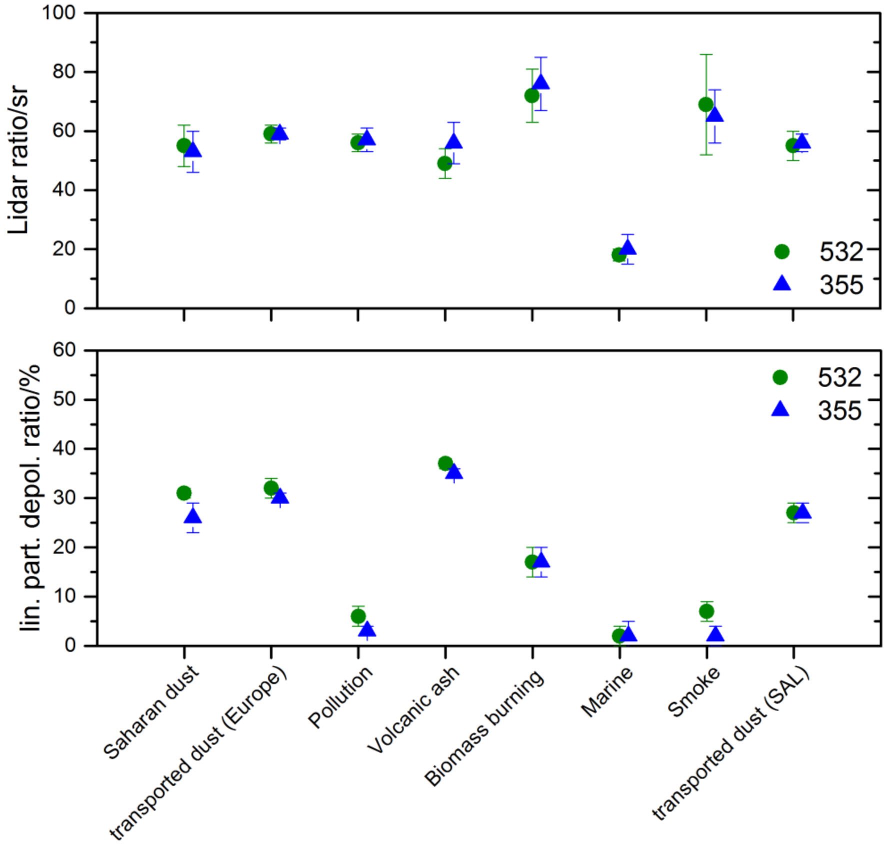

Figure 48: Mean values of the lidar ratio and the particle linear depolarization ratio for the measurements shown in Figure 47. The error bars show the standard deviation of the mean values.

The wavelength dependence of the particle linear depolarization ratio of Saharan dust was analysed in detail during the SAMUM-1 and SAMUM-2 project. Lidar measurements at different wavelengths as well as model calculation in consideration of the non-spherical shape of the dust particles were performed. Wavelength dependence was found for pure and fresh Saharan air layers close to its source regions over the Saharan desert during SAMUM-1 (Freudenthaler et al., 2009) as well as for the Saharan air layer at the beginning of its long-range transport measured during SAMUM-2 at Cape Verde (Groß et al., 2011). Modelling the intensive optical properties of Saharan dust under consideration of its non-spherical shape also showed wavelength dependence for the particle linear depolarization ratio at 355 and 532 nm (Gasteiger et al., 2011a). The model results agreed well with the measured values. The intensive optical properties for long-range transported Saharan dust were studied in the framework of EARLINET at the Munich/Maisach EARLINET site (Wiegner et al., 2011) and during the Saharan Aerosol Long-range Transport and Aerosol-Cloud-Interaction Experiment

(SALTRACE; Weinzierl et al., 2016) at Barbados (Groß et al., 2015b). During both measurement events we found a change in the wavelength dependency of the particle linear depolarization ratio. However this change is quite different for the different transport paths. While we found higher mean values at both wavelengths (355 and 532 nm) over Europe, we found slightly lower values at 532 nm compared to those of fresh dust over Barbados. At both locations we saw no wavelength dependence of the particle linear depolarization ratio of long-range transported Saharan dust.

For smoke aerosols we found small wavelength dependence of the particle linear depolarization ratio with slightly smaller values at 355 nm. However, the mean values of both wavelengths are smaller than 0.1. Using multi-wavelength airborne measurements Burton et al., (2015) also found a wavelength dependence of the particle linear depolarization ratio of smoke. However they found larger values at 355 nm. Reported values of the particle linear depolarization ratio of smoke are quite variable and the causes of depolarization by smoke aerosols is not well understood. In general the different values are explained by two effects: either the irregular shape of the smoke particles or by the entrainment of soil dust during the lifting processes (Burton et al., 2015). Another effect might result from alteration during transport and aging which was e.g. found for the lidar ratio (Amiridis et al., 2009).

Table 7: Mean values of the linear particle depolarization and lidar ratio for different aerosol types measured at 355 and 532 nm and for aerosol classification in the referenced publications. ±–values give the standard deviation of the mean.

Aerosol type	δ_{355}	δ_{532}	LR_{355} [sr]	LR_{532} [sr]	References
dust	0.26 ± 0.03	0.31 ± 0.01	53 ± 7	55 ± 7	Tesche et al., 2009a; Freudenthaler et al., 2009; Groß et al., 2011
Transp. Dust (Europe)	0.3 ± 0.02	0.32 ± 0.02	59 ± 2	59 ± 3	Wiegner et al., 2011
Pollution	0.03 ± 0.01	0.06 ± 0.02	57 ± 4	56 ± 3	Groß et al., 2013a; Illingworth et al., 2016
Volcanic ash	0.35 ± 0.01	0.37 ± 0.01	56 ± 7	49 ± 5	Groß et al., 2012
Biomass burning	0.17 ± 0.03	0.17 ± 0.03	76 ± 9	72 ± 9	Groß et al., 2011
Marine	0.02 ± 0.02	0.02 ± 0.02	20 ± 5	18 ± 2	Groß et al., 2011; Groß et al., 2015
Smoke	0.02 ± 0.02	0.07 ± 0.02	65 ± 9	69 ± 17	Groß et al., 2013b; Illingworth et al., 2016
Transp. Dust (Caribbean)	0.27 ± 0.02	0.27 ± 0.02	56 ±3	55 ± 5	Groß et al., 2015

The mean values of the particle linear depolarization ratio and lidar ratio found for the different aerosol types in the referenced studies are summarized in Table 7.

8.2 Extinction and backscatter measurements

For assessing the wavelength dependence of the extinction coefficient measured by lidar systems at 355 and 532 nm we take advantage of a number of sun-photometer measurements performed in different aerosol conditions. The main aerosol types are summarized in Figure 49.

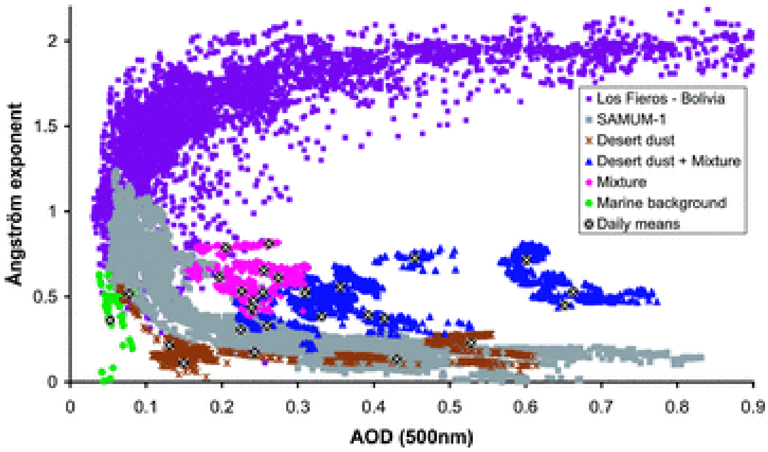

Figure 49: Scatter plot of Angström Exponent vs. aerosol optical depth at 500 nm derived from sun-photometer and lidar measurements during SAMUM-1 in Morocco and SAMUM-2 at Cape Verde. Measurements in Bolivia are taken from Holben et al., 2001. Figure adopted from Toledano et al., 2011.

While large particles, e.g. Saharan dust and marine aerosols, show small values for the Angström Exponent between 380 and 500 nm between about 0.01 and 0.5 and thus no or almost no wavelength dependency of the extinction coefficient of those particles between 355 and 532 nm. Smaller particles like smoke aerosols (in Figure 49 from fires in Bolivia) show larger values for the Angström Exponent of > 1. Most values even exceed 1.5. For the measurements of fresh Saharan dust a mean Angström Exponent of 0.2 was reported (Freudenthaler et al., 2009; Toledano et al., 2009) and for smoke plumes observed during SAMUM-2 the majority of observed Angström Exponents between 355 and 532 nm was > 1.0 with a maximum at 1.25. Table 1 and Figure 50 summarize the Angström Exponents of different aerosol types derived from sun-photometer and lidar measurements found in literature.

Table 8: Angström Exponents (380/500 and 355/532) and corresponding references for different aerosol types derived from sun-photometer and lidar measurements.

Aerosol type	Angström Exponent	References
dust	0.2 – 0.3	Freudenthaler et al., 2009; Tesche et al., 2009; Toledano et al., 2009; Toledano et al, 2011; Groß et al., 2015b
Pollution	1.1 – 1.7	Müller et al., 2007; Toledano et al., 2007
Volcanic ash	~0.1	Gasteiger et al., 2011b; Groß et al., 2012
Biomass burning	0.7 – 0.8	Müller et al., 2007; Tesche et al., 2011
Marine	0.1 – 0.3	Müller et al., 2007; Toledano et al., 2011
Smoke	> 1.0	Holben et al., 2001; Müller et al., 2007; Tesche et al., 2009b

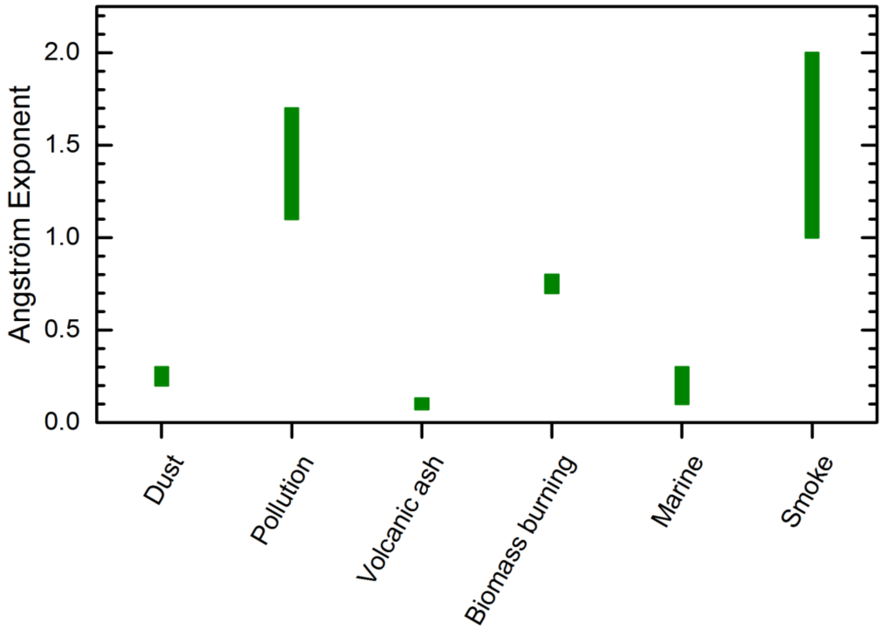

Figure 50: Anström Exponents (355/532) found for different types of aerosols as summarized in Table 8.

A less studied property when looking at the wavelength dependence of the lidar profiles is the color ratio (i.e. the ratio of the backscatter coefficient at 355 nm and the backscatter coefficient at 532 nm). Only few papers refer to this property. Table 9 summarizes the values found in literature. Values around 1.0 are found for rather large particles like dust aerosols, sea salt in the marine boundary layer or volcanic ash. Small particles like pollution or smoke aerosols show larger values >1.5 and are thus an indication for wavelength dependent backscatter coefficient profiles considering measurements at 355 and 532 nm.

Table 9: Color ratio (355/532) and corresponding references for different aerosol types derived from lidar measurements.

Aerosol type	Color ratio	References
dust	1.0 – 1.2	Groß et al., 2013; Tesche et al., 2009b; Tesche et al., 2011a
Pollution	~ 1.6	Tesche et al., 2009b
Volcanic ash	~1	Ansmann et al., 2010; Groß et al., 2012
Biomass burning	1.9 – 2.0	Müller et al., 2007
Marine	1.0 – 1.2	Groß et al., 2011; Tesche et al., 2011
Smoke	1.5 – 1.7	Tesche et al., 2009b; Amiridis et al., 2009

Conclusion

Looking at different optical parameters measurements at 355 and 532 nm partly show differences. For direct comparisons of optical properties it is thus helpful to have a first guess on the observed aerosol type. An important point considering these differences is that they differently influence the conversion in higher level products, e.g. aerosol classification, so that a different wavelength would provide independent measurements particularly with respect to validation of higher level products.

References

Amiridis, V., Balis, D. S., Giannakaki, E., Stohl, A., Kazadzis, S., Koukouli, M. E., and Zanis, P.: Optical characteristics of biomass burning aerosols over Southeastern Europe determined from UV-Raman lidar measurements, Atmospheric Chemistry and Physics, 9(7), 2431-2440, 2009.

Ansmann, A., Tesche, M., Groß, S., Freudenthaler, V., Seifert, P., Hiebsch, A., ... and Wiegner, M.: The 16 April 2010 major volcanic ash plume over central Europe: EARLINET lidar and AERONET photometer observations at Leipzig and Munich, Germany, Geophysical Research Letters, 37(13), 2010.

Baars, H., Ansmann, A., Althausen, D., Engelmann, R., Heese, B., Müller, D., ... and Souza, R.: Aerosol profiling with lidar in the Amazon Basin during the wet and dry season, Journal of Geophysical Research: Atmospheres, 117(D21), 2012.

Barker, H. W., Jerg, M. P. Wehr, T., Kato, S., Donovan, D. P., and Hogan R. J.: A 3D cloud-construction algorithm for the EarthCARE satellite mission, Q. J. R. Meteorol. Soc., 137, 1042-1058, 2011.

Burton, S. P., Ferrare, R. A., Hostetler, C. A., Hair, J. W., Rogers, R. R., Obland, M. D., ... and Froyd, K. D.: Aerosol classification using airborne High Spectral Resolution Lidar measurements-methodology and examples, Atmospheric Measurement Techniques, 5(1), 73, 2012.

Burton, S. P., Hair, J. W., Kahnert, M., Ferrare, R. A., Hostetler, C. A., Cook, A. L., ... and Fenn, M. A.: Observations of the spectral dependence of linear particle depolarization ratio of aerosols using NASA Langley airborne High Spectral Resolution Lidar, Atmospheric Chemistry and Physics, 15(23), 13453-13473, 2015.

Brown, P. R. A., and P. N. Francis: Improved measurements of the ice water content in cirrus using a total-water probe, J. Atmos. Oceanic Technol., 12, 410–414, 1995.

Delanoë, J., A. Protat, J. Testud, D. Bouniol, A. J. Heymsfield, A. Bansemer, P. R. A. Brown, and R. M. Forbes: Statistical properties of the normalized ice particle size distribution, J. Geophys. Res., 110, D10201, doi:10.1029/2004JD005405, 2005.

Delanoë, J., and Hogan R. J.: A variational scheme for retrieving ice cloud properties from combined radar, lidar, and infrared radiometer, J. Geophys. Res., 113, D07204, doi:10.1029/2007JD009000, 2008.

Delanoë, J. and Hogan, R. J.: Combined CloudSat-CALIPSO-MODIS retrievals of the properties of ice clouds, Journal of Geophysical Research: Atmospheres, 115(D4), 2010.

Delanoë, J. M. E., Heymsfield, A. J., Protat, A., Bansemer, A., and Hogan, R. J.: Normalized particle size distribution for remote sensing application, Journal of Geophysical Research: Atmospheres, 119(7), 4204--4227, 2014.

Engelmann, R., Kanitz, T., Baars, H., Heese, B., Althausen, D., Skupin, A., Wandinger, U., Komppula, M., Stachlewska, I. S., Amiridis, V., Marinou, E., Mattis, I., Linné, H., and Ansmann, A.: The automated multiwavelength Raman polarization and water-vapor lidar PollyXT: the neXT generation, Atmos. Meas. Tech., 9, 1767-1784, doi:10.5194/amt-9-1767-2016, 2016.

Esselborn, M., Wirth, M., Fix, A., Tesche, M., and Ehret, G.: Airborne high spectral resolution lidar for measuring aerosol extinction and backscatter coefficients, Appl. Opt., 47, 346–358, doi:10.1364/AO.47.000346, 2008.

Francis, P. N., P. Hignett, and A. Macke: The retrieval of cirrus cloud properties from aircraft multi-spectral reflectance measurements during EUCREX’93, Q. J. R. Meteorol. Soc., 124, 1273–1291, 1998.

Freudenthaler, V., Esselborn, M., Wiegner, M., Heese, B., Tesche, M., Ansmann, A., ... and Ehret, G.: Depolarization ratio profiling at several wavelengths in pure Saharan dust during SAMUM 2006, Tellus B, 61(1), 165-179, 2009.

Gasteiger, J., Wiegner, M., Groß, S., Freudenthaler, V., Toledano, C., Tesche, M., & Kandler, K.: Modelling lidar-relevant optical properties of complex mineral dust aerosols, Tellus B, 63(4), 725-741, 2011a.

Gasteiger, J., Groß, S., Freudenthaler, V., and Wiegner, M.: Volcanic ash from Iceland over Munich: mass concentration retrieved from ground-based remote sensing measurements, Atmospheric chemistry and physics, 11(5), 2209-2223, 2011b.

Groß, S., Tesche, M., Freudenthaler, V., Toledano, C., Wiegner, M., Ansmann, A., ... and Seefeldner, M.: Characterization of Saharan dust, marine aerosols and mixtures of biomass-burning aerosols and dust by means of multi-wavelength depolarization and Raman lidar measurements during SAMUM 2, Tellus B, 63(4), 706-724, 2011.

Groß, S., Freudenthaler, V., Wiegner, M., Gasteiger, J., Geiß, A., and Schnell, F.: Dual-wavelength linear depolarization ratio of volcanic aerosols: Lidar measurements of the Eyjafjallajökull plume over Maisach, Germany, Atmospheric Environment, 48, 85-96, 2012.

Groß, S., Esselborn, M., Weinzierl, B., Wirth, M., Fix, A., and Petzold, A.: Aerosol classification by airborne high spectral resolution lidar observations, Atmospheric Chemistry and Physics, 13(5), 2487-2505, 2013.

Groß, S., Freudenthaler, V., Wirth, M., and Weinzierl, B.: Towards an aerosol classification scheme for future EarthCARE lidar observations and implications for research needs, Atmospheric Science Letters, 16(1), 77-82, 2015a.

Groß, S., Freudenthaler, V., Schepanski, K., Toledano, C., Schäfler, A., Ansmann, A., and Weinzierl, B.: Optical properties of long-range transported Saharan dust over Barbados as measured by dual-wavelength depolarization Raman lidar measurements, Atmos. Chem. Phys., 15(11), 067-11, 2015b.

Hartmann, D. L., Ockert-Bell, M. E., and Michelsen, M. L.: The Effect of Cloud Type on Earth's Energy Balance: Global Analysis, J. Climate, 5, 1281–1304, 1992.

Heymsfield, A. J., Schmitt, C., Bansemer, A., & Twohy, C. H.: Improved representation of ice particle masses based on observations in natural clouds. Journal of the Atmospheric Sciences, 67(10), 3303-3318, 2010.

Hogan, R. J., Tian, L., Brown, P. R., Westbrook, C. D., Heymsfield, A. J., and Eastment, J. D.: Radar scattering from ice aggregates using the horizontally aligned oblate spheroid approximation. Journal of Applied Meteorology and Climatology, 51(3), 655-671, 2012.

Holben, B., Tanre, D., Smirnov, A., Eck, T., Slutsker, I. …: An emerging ground-based aerosol climatology: aerosol optical depth from AERONET, J. Geophys. Res. 106, 12067–12097, 2001.

Intrieri, J. M., Stephens, G. L., Eberhard, W. L., and Uttal, T.: A Method for Determining Cirrus Cloud Particle Sizes Using Lidar and Radar Backscatter Technique, Journal of Applied Meteorology, 32, 1074–1082, 1993.

Illingworth, A. J., Barker, H. W., Beljaars, A., Ceccaldi, M., Chepfer, H., Clerbaux, N., ... and Fukuda, S.: The EarthCARE satellite: The next step forward in global measurements of clouds, aerosols, precipitation, and radiation, Bulletin of the American Meteorological Society, 96(8), 1311-1332, 2015.

Li, L., Heymsfield, G. M., Tian, L., and Racette, P. E.: Measurements of ocean surface backscattering using an airborne 94-GHz cloud radar—Implication for calibration of airborne and spaceborne W-band radars, Journal of Atmospheric and Oceanic Technology, 22(7), 1033-1045, 2005.

Mech, M., Orlandi, E., Crewell, S., Ament, F., Hirsch, L., Hagen, M., Peters, G., and Stevens, B.: HAMP - the microwave package on the High Altitude and LOng range research aircraft HALO, **Atmospheric** Measurement Techniques Discussions, 7, 4623–4657, doi:10.5194/amtd-7-4623-2014, 2014.

Mitchell, D. L., Rasch, P., Ivanova, D., McFarquhar, G., and Nousiainen, T.: Impact of small ice crystal assumptions on ice sedimentation rates in cirrus clouds and GCM simulations. Geophysical Research Letters, 35(9), 1996.

Müller, D., Ansmann, A., Mattis, I., Tesche, M., Wandinger, U., Althausen, D., and Pisani, G.: Aerosol-type-dependent lidar ratios observed with Raman lidar, Journal of Geophysical Research: Atmospheres, 112(D16), 2007.

Platt, C. M. R., Young, S. A., Austin, R. T., Patterson, G. R., Mitchell, D. L., and Miller, S. D.: LIRAD observations of tropical cirrus clouds in MCTEX. Part I: Optical properties and detection of small particles in cold cirrus. Journal of the atmospheric sciences, 59(22), 3145-3162, 2002.

Stephens, G. L., Vane, D. G., Boain, R. J., Mace, G. G., Sassen, K., Wang, Z., ... and Miller, S. D.: The CloudSat mission and the A-Train: A new dimension of space-based observations of clouds and precipitation, Bulletin of the American Meteorological Society, 83(12), 1771-1790, 2002.

Szyrmer, W., Tatarevic, A., and Kollias, P.: Ice clouds microphysical retrieval using 94-GHz Doppler radar observations: Basic relations within the retrieval framework. Journal of Geophysical Research: Atmospheres, 117(D14), 2012.

Tesche, M., Ansmann, A., Müller, D., Althausen, D., Mattis, I. N. A., Heese, B., ... and Knippertz, P.: Vertical profiling of Saharan dust with Raman lidars and airborne HSRL in southern Morocco during SAMUM, Tellus B, 61(1), 144-164, 2009a.

Tesche, M., Ansmann, A., Müller, D., Althausen, D., Engelmann, R., Freudenthaler, V., & Groß, S.: Vertically resolved separation of dust and smoke over Cape Verde using multiwavelength Raman and polarization lidars during Saharan Mineral Dust Experiment 2008, Journal of Geophysical Research: Atmospheres, 114(D13), 2009b.

Tesche, M., Gross, S., Ansmann, A., Mueller, D., Althausen, D., Freudenthaler, V., and Esselborn, M.: Profiling of Saharan dust and biomass-burning smoke with multiwavelength polarization Raman lidar at Cape Verde, Tellus B, 63(4), 649-676, 2011.

Testud, J., Oury, S., Black, R. A., Amayenc, P., and Dou, X.: The concept of “normalized” distribution to describe raindrop spectra: A tool for cloud physics and cloud remote sensing. Journal of Applied Meteorology, 40(6), 1118-1140, 2001.

Toledano, C., Cachorro, V. E., Berjon, A., De Frutos, A. M., Sorribas, M., De la Morena, B. A., and Goloub, P.: Aerosol optical depth and Ångström exponent climatology at El Arenosillo AERONET site (Huelva, Spain), Quarterly Journal of the Royal Meteorological Society, 133(624), 795-807, 2007.

Toledano, C., Wiegner, M., Garhammer, M., Seefeldner, M., Gasteiger, J., Müller, D., and Koepke, P.: Spectral aerosol optical depth characterization of desert dust during SAMUM 2006, Tellus B, 61(1), 216-228, 2009.

Toledano, C., Wiegner, M., Groß, S., Freudenthaler, V., Gasteiger, J., Müller, D., ... and O'neill, N. T.: Optical properties of aerosol mixtures derived from sun-sky radiometry during SAMUM-2, Tellus B, 63(4), 635-648, 2011.

Warren, S., Hahn, C., London, J., Chervin, R., and Jenne, R.: Global Distribution of Total Cloud Cover and Cloud Type Amounts Over Land, NCAR Tech. Note NCAR/TN-317+STR, p. 42, doi:10.5065/D6GH9FXB, 1986.

Weinzierl, B., Ansmann, A., Prospero, J. M., Althausen, D., Benker, N., Chouza, F., ... and Gasteiger, J.: The Saharan Aerosol Long-range Transport and Aerosol-Cloud-Interaction Experiment (SALTRACE): overview and selected highlights, Bulletin of the American Meteorological Society, 2016.

Winker, D., Vaughan, M., Omar, A., Hu, Y., Powell, K., Liu, Z., Hunt, W., and Young, S.: Overview of the CALIPSO Mission and CALIOP Data Processing Algorithms. J. Atmos. Oceanic Technol., 26, 2310–2323, doi: 10.1175/2009JTECHA1281.1, 2009.

Wiegner, M., Groß, S., Freudenthaler, V., Schnell, F., and Gasteiger, J.: The May/June 2008 Saharan dust event over Munich: Intensive aerosol parameters from lidar measurements, Journal of Geophysical Research: Atmospheres, 116(D23), 2011.

Wirth, M., Fix, A., Mahnke, P., Schwarzer, H., Schrandt, F., and Ehret, G.: The airborne multi-wavelength water vapor differential absorption lidar WALES: system design and performance, Applied Physics B, 96, 201–213, doi:10.1007/s00340-009-3365-7, 2009.